



PCCP

**Pattern-illumination Time-resolved Phase Microscopy and
its Applications for Photocatalytic and Photovoltaic
Materials**

Journal:	<i>Physical Chemistry Chemical Physics</i>
Manuscript ID	CP-REV-12-2023-006211.R1
Article Type:	Review Article
Date Submitted by the Author:	04-Feb-2024
Complete List of Authors:	Katayama, Kenji; Chuo University, Department of Chemistry; Kagaku Gijutsu Shinko Kiko, Precursory Research for Embryonic Science and Technology

SCHOLARONE™
Manuscripts

Pattern-illumination Time-resolved Phase Microscopy and its Applications for Photocatalytic and Photovoltaic Materials

Kenji Katayama^{1*}

¹ Department of Applied Chemistry, Chuo University, Tokyo 112-8551, Japan;

*Corresponding authors:

K. Katayama, Phone: +81-3-3817-1913, E-mail: kkata@kc.chuo-u.ac.jp

Abstract

The pattern-illumination time-resolved phase microscopy (PI-PM) method is a technique used to study the microscopic charge carrier dynamics in photocatalytic and photovoltaic materials. The method involves illuminating a sample with a pump light pattern, which generates and decays charge carriers due to trapping, recombination, and transfer processes. The distribution of photo-excited charge carriers is observed through refractive index changes using phase-contrast imaging. In the PI-PM method, refractive index change is selectively monitored by adjusting the focus position and enhance sensitivity to the phase change of photo-excited charge carriers, providing the observation of non-radiative processes, such as charge diffusion, trapping to defect/surface states, and interfacial charge transfer of photocatalytic and photovoltaic reactions. The quality of the image sequence is recovered using various informatics calculation. Categorizing and mapping different types of charge carriers based on their response profiles using clustering analysis, provides spatial information on charge carrier types, and the identification of local sites for efficient and inefficient photo-induced reactions, providing valuable information for the design and optimization of photocatalytic materials such as the cocatalyst effect.

Keywords: photocatalyst, titanium oxide, hematite, bismuth vanadate, strontium titanium oxide, time-resolved microscopy, perovskite, image recovery, clustering, charge carrier dynamics

1. Introduction

The global demand for solar devices has been increasing due to their potential to vastly exceed human energy needs. Focus is on affordable, easily processed solar cells¹⁻³ like perovskite⁴⁻⁶ and sensitized solar cells⁷⁻⁹, as well as photocatalysts used for decomposing pollutants¹⁰⁻¹² and splitting water into oxygen and hydrogen.¹³⁻¹⁷ Various materials, including oxides and sulfides (e.g., TiO₂, Fe₂O₃, Cu₂O, PbS, CdS, CdSe)¹⁸, and structures (rods, tubes, inverse opal structures) are employed to enhance surface area and charge carrier transport.¹⁹

In photovoltaic and photocatalytic devices, oxide and sulfide semiconductor particles are crucial for generating photo-excited carriers, and for charge transport and separation. The effectiveness of these devices depends on efficiently separating and utilizing photo-excited charge carriers, while minimizing loss due to recombination or trapping.²⁰ For example, in water splitting photocatalytic systems, these carriers are used in reduction and oxidation reactions for hydrogen and oxygen generation. Understanding and improving the lifetime and transport properties of these carriers is essential for enhancing device efficiency and preventing recombination.

However, only the measurements of lifetime and transport properties cannot solve the issues due to the complexity of the materials' structures. Unlike single crystals, which can be easily referenced from literature for their physical properties like lifetime and mobility, the layers in photo-devices are often porous and rough, made from nanoparticles.^{17,21} This results in millions of interfaces, aggregates, cracks, and scratches at various scales on a macroscopic scale, significantly affecting charge carrier behavior. Various photocatalytic materials show multi-order exponential decay of photo-excited charge carriers from femtoseconds to milliseconds, such as TiO₂,²²⁻²⁵ SrTiO₃,^{26,27} BiVO₄,²⁸ WO₃,²⁹ and Fe₂O₃.³⁰⁻³²

In photocatalytic applications using particulate aggregates of semiconductor particles, the film surfaces and interfaces composed of these particles lead to various lifetimes of charge carriers due to trap states. This trapping and decay cause a reduction in energy and reaction efficiencies for photovoltaics and photocatalysts due to recombination and deactivation. The dynamics of charge carriers in these particulate films are markedly different from those in crystalline forms. For instance, while a single-crystalline TiO₂ exhibits a single exponential decay³³, particulate films show multiple different decays over various time scales,^{22,34-37} indicating a complex and varied charge carrier behavior in these materials.

The semiconductor particles used in photo-devices, either sourced from manufacturers or synthesized in labs as powders, are coated on substrates and calcined, which introduces a wide range of defects across various scales. This leads to challenges in determining which photo-excited charge carriers are reactive or non-reactive, requiring detailed studies with specific techniques like electron/hole scavengers.^{36,37} In dye-sensitized solar cells, the decay of excited electrons from dyes to

semiconductor films follows a stretched exponential function, indicating inhomogeneous processes.³⁸ In hematite, used for water splitting, charge carriers show a non-exponential decay with long lifetimes, which are dependent on the applied bias voltage.³⁹

The dynamics of these photo-excited charge carriers are typically studied using techniques like time-resolved photoluminescence (TP),^{40–45} transient absorption (TA),^{20,33,45–58} and time-resolved microwave conductivity (TMC).^{59,60} TP is sensitive to the emission of excited carriers but overlooks non-emissive processes. TA can observe various charge carriers but lacks the sensitivity of TP and faces challenges in wavelength selection. TMC focuses on mobile charge carriers but does not provide information on trapped carriers. Each of these methods has its own strengths and limitations and is chosen based on the specific requirements of the study and available resources.

The observations made via refractive index changes offer different insights compared to those obtained through TP or TA, especially for particulate samples. The sensitivity of these methods to dipole changes at interfaces makes them preferable for monitoring charge carriers at these locations,^{61,62} contributing significantly to the understanding of charge carrier dynamics.

To properly understand the issue, merely looking at the average temporal response of charge carriers is inadequate. It is crucial to study these carriers in a localized manner, taking into account their structural and positional context. In particulate films, charge carriers often get trapped at different defect sites and exhibit a range of lifetimes. As a result, they may be both confined locally and capable of transport.

TA microscopy is a well-established method⁶³ used to study nanomaterials and the diffusion of photo-excited carriers in materials like silicon nanowire and perovskite thin films.^{55,56,64,65} This technique analyzes charge carrier diffusion by observing the shape change of a spot illuminated by focused pump light on an ultrafast timescale.^{57,64,66,67} TA microscopy has been further improved by integrating it with super-resolution microscopy methods like stimulated emission depletion (STED)⁶⁸ and structured illumination,^{69,70} allowing observation of smaller regions at faster timescales. However, its application is limited to timescales within nanoseconds and small-area observation. Furthermore, the focus position must be accurately adjusted at each spot, and it is difficult to apply this method for the particulate films with a rough surface. Photoluminescence microscopy is another method where light emitted from photo-excited carriers is mapped to identify charge trapping locations.⁷¹ While useful, this technique captures only a part of the charge carrier dynamics due to no-response of non-radiative processes. Ultrafast electron microscopy offers another approach to study the spatio-temporal dynamics of photo-excited charge carriers^{72–75} and has been applied to nanotube and nanoparticulate films.⁷⁶ This technique is limited by the availability of ultrashort electron pulses and the need for vacuum conditions, making it challenging to use under operational conditions of photo-devices.

We have studied on the dynamics of charge carriers in dye or quantum-dot-sensitized solar cells,^{62,77,77,78} and water splitting photoanode materials.^{31,32} The transient grating (TG) method^{79,80} is

a key technique used, where the refractive index change is monitored to study the dynamics of photo-excited carriers. This method is particularly sensitive to dipole changes at interfaces, making it suitable for examining charge transfer dynamics there.

To analyze the inhomogeneity in the decay processes of charge carriers, a nonlinear least square analysis with maximum entropy (ME) regularization⁸¹ is introduced. This approach provides a distribution of decay times, rather than a single decay time, which is more fitting, given the broad distribution of lifetimes in photo-devices. This method has been applied to investigate photocatalysis,⁷⁸ water splitting,³¹ charge carrier dynamics in sensitized solar cells,^{82,83} charge separation at interfaces,^{61,84} offering a deeper understanding of charge dynamics in these inhomogeneous samples.

In addition to the heterodyne-TG method,^{79,80} the pattern-illumination time-resolved phase microscopy (PI-PM)^{25,85} have been developed to observe charge carrier dynamics through refractive index changes.^{61,86} The patterned-illumination, similar as the TG method, features the utilization of the contrast between the light illuminated and non-illuminated region, to enhance the difference of the effect between them, which effectively used in the image recovery calculations in the data science. This technique has been applied to study various types of photocatalysts and solar cells. The PI-PM method has been used to clarify the spatially-resolved catalytic activity on a micro-scale,⁸⁷ with a support of the image recover and clustering calculations, providing physical and chemical insights into spatially-resolved inhomogeneity of different charge carrier types and photo-catalytic activity on a micro-scale. Here, we review the development of the PI-PM method and the informatics calculations used, followed by several applications for studying the photocatalytic and photovoltaic materials by clarifying the local charge carrier dynamics.

2. Analysis and equipment

2.1 Optical setup and technical advantage

The optical setup features how to make a contrast between the irradiated and non-irradiated regions, which enhances the contrast of the effect and favorable for the image recovery calculation. Figure 1A illustrates the initial configuration of the PI-PM technique. Initially, an excitation pulse is directed through a grating, creating an image pattern at the sample's location. This is achieved using a 4f setup comprising two lenses with distinct focal lengths (38 mm and 80 mm), resulting in a fringe spacing on the sample that is half of the original spacing. The sample is then excited by a pump pulse, leading to the creation of photo-excited carriers and subsequent heat from carrier decay. This heat changes the refractive index, mirroring the pattern of the pump light. Subsequently, a probe pulse, delayed relative

to the pump pulse, is directed at the sample to illuminate it. This probe pulse, upon passing through the sample, is partially diffracted and then transmitted through another pair of lenses with focal lengths of 60 mm and 1000 mm, achieving an expansion ratio of 17. This setup allows the sample to be imaged onto a CMOS camera. The probe beam is expanded to a size larger than the CMOS camera's sensor area, and only its central part is used for imaging. The sequence of PI-PM images is captured by varying the time delay with a function generator, allowing for a collection of images at different intervals.

The third harmonics of a Nd:YAG pulse laser (with a 5 ns pulse width and 355 nm wavelength) provided by GAIA, Rayture Systems, served as the pump light, while the probe light came from the second harmonics of another Nd:YAG pulse laser (also 5 ns pulse width but with a 532 nm wavelength) from the same provider. The synchronization of these pulses was managed by two function generators (WF1968, NF), both triggered by a base clock (DF1906, NF). These generators were responsible for timing both the flash lamp and the Q-switch, offering a precision of 100 ps. The pump pulse covered an area with a diameter of 5 mm. The intensities of the pump and probe lights were 0.8 mJ/pulse and 0.02 mJ/pulse, respectively. A grating with a spacing of 40 μm was employed for the measurements. However, due to the optics used to reduce it, the grating spacing at the sample was effectively 19 μm . The CMOS camera used (MV1-D1024E-160, Photon Focus) featured a sensor area of 10.9x10.9mm (1024x1024 pixels), but only a central vertical strip (200x1024 pixels) was utilized in order to lessen the data processing load. To demonstrate the measurement technique, a stripe pattern identical to the transient grating excitation was used.⁸⁸

Using a standard fast CMOS camera for image acquisition confines the time resolution to milliseconds, inadequate for observing the dynamics of photo-excited charge carriers. Moreover, as the camera's time resolution tightens through reduced exposure times, the signal-to-noise (S/N) ratio deteriorates due to a decrease in photon count in such rapid imaging. These issues can be addressed by employing the pump-probe pulse imaging method. In this technique, the time resolution is determined by the width of the pulse, and the photon count remains unaffected, as photons are concentrated within the duration of the pulse. The temporal resolution of this setup was constrained solely by the probe light's pulse width, which is 5 ns. By altering the time delay between the pump and probe pulses, a series of images were captured and stored on a computer.

In the revised PI-PM arrangement depicted in Figure 1B, the pump pulse light undergoes reflection via a digital micromirror device (DMD) (DLP4500, Texas Instruments), with the pattern being modifiable through computer control. The DMD mirror consists of 1039680 mirrors, each 7.6 μm , arranged in 912 columns by 1140 rows with the diamond pixel array geometry with a 0.45 inch diagonal length. Each micro-mirrors are controlled to on/off directions to obtain the designated image. The reflection from the DMD is transferred using a lens ($f = 100$ mm) and an objective lens (LUCPLFLN20x, Olympus), shrinking the pattern to 1/14th of its original size on the sample. This

pulsed illumination is combined with the pump light at a dichroic mirror for sample illumination. The light that passes through the sample is then captured using another objective lens (LUCPLFLN20x, Olympus) and a tube lens (TTL180-A, Thorlabs). A CMOS camera (MV1-D1024E-160, Photon Focus) with a sensor area measuring 10.9 mm x 10.9 mm (1024 x 1024 pixels) is employed for image acquisition. To alleviate computational demands, only a central vertical section (200 x 1024 pixels) of each image is recorded. The images are averaged between three to five times, depending on the signal-to-noise (S/N) ratio, and capturing each image takes about 5 to 10 seconds.

Figure 2 displays sequences of images for both line-pattern and dot-pattern excitations in a TiO₂ nanoparticulate film. The variation in the film's refractive index, resulting from the decay of photo-excited carriers, was distinctly visible. The width of the lines and the diameter of the dots, representing the refractive index changes caused by these carriers, and the contrast was sufficiently distinct to allow for an analysis of the distribution of charge carriers. The spatial resolution was 3 μm .

One of the hidden advantage of this method is providing a whole image acquisition instead of point-scanning. In this technique, a patterned pump light illumination is used to apply the image recovery calculation in informatics theory to the observed images, and the phase-contrast imaging is used instead of the absorption change measurement. By utilizing the image recovery, the signal-to-noise ratio is improved to obtain a slight change of the images due to photo-induced change, and this method could extend the time-resolved sequence until the millisecond order.^{25,85}

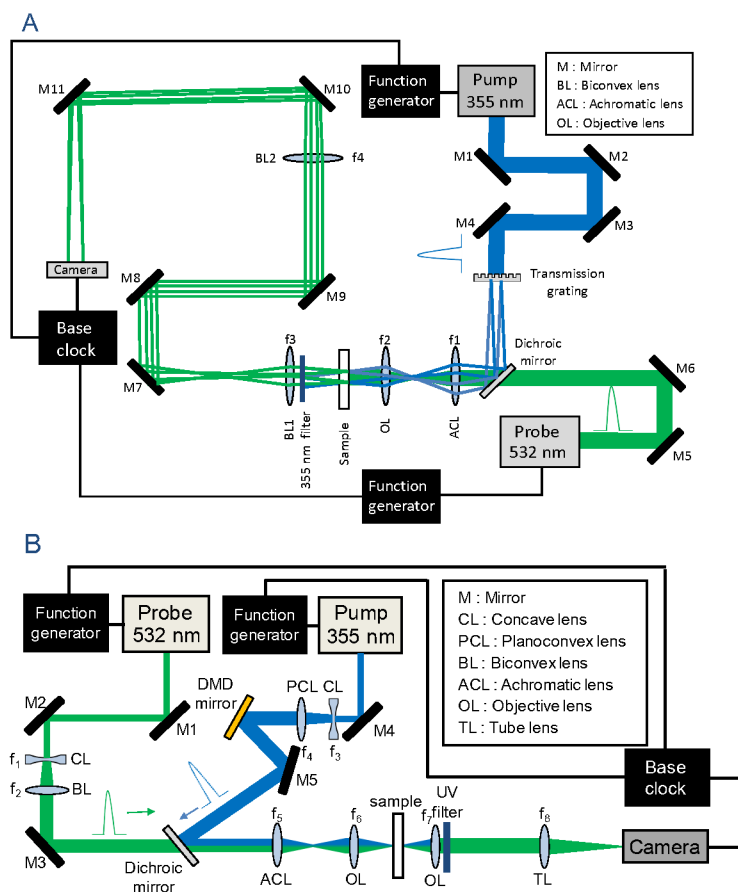


Figure 1 The schematic overview of the optical setups of the PI-PM method are shown in the former (A) and the latest versions (B). **A:** A pump pulse was first diffracted by a transmission grating and the striped pattern was projected on the sample using the 4f configuration of two lenses with different focal lengths ($f_1 = 80$, $f_2 = 38$ mm). Another probe pulse was irradiated onto the sample after collimation by the f_1 and f_2 lenses and the probe light is diffracted by the pattern. For imaging, additional two lenses with different focal lengths ($f_3 = 60$ mm, $f_4 = 1000$ mm) were set up behind the sample to magnify the sample image to the camera. **B:** A pump pulse was first reflected to the DMD mirror which can draw any pattern as we like. In most of measurements, square patterns were drawn on the DMD mirror and projected on the sample. Another probe pulse was irradiated onto the sample. For the imaging purpose, additional two lenses with different focal lengths were set up behind the sample. Reproduced from ref. 25,85 with permission from American Institute of Physics, copyright 2019, 2020.

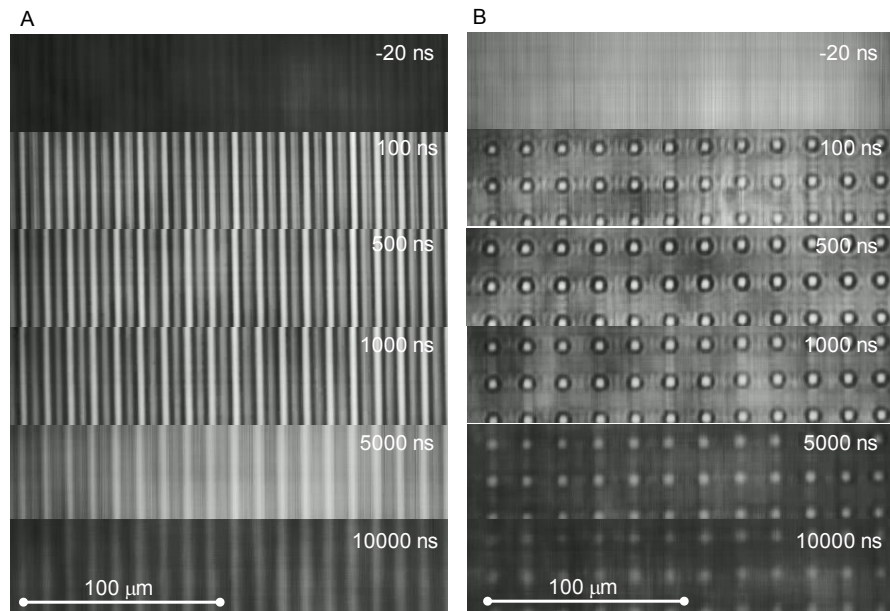


Figure 2 Examples of the image sequences of a TiO_2 film measured by the PI-PM method; **A**: line-pattern photo-excitation and **B**: dot-pattern photo-excitation. Reproduced from ref. 85 with permission from American Institute of Physics, copyright 2020.

2.2 Defocus induced phase-contrast image enhancement and fast image acquisition

This section describes how to detect the contrast of the refractive index change, which cannot be detected with an image contrast, because the phase change due to the refractive index change does not alter the image intensity change. The method of detecting the phase change due to the refractive index change is explained in this section.

The pump pulse's stripe pattern is projected onto a sample, creating photo-excited charge carriers in a pattern identical to that of the pump pulse. As the refractive index varies with the quantity and effective mass of these carriers, a corresponding refractive index pattern emerges within the sample. In the PI-PM imaging method, as illustrated in Figure 3A, light shone on the sample is locally altered or deflected (diffracted) due to the refractive index pattern. This results in the transformation of the phase image (which depicts the change in refractive index) into an intensity image. This intensity pattern is then captured by imaging optics and recorded on an imaging device.

Imaging the refractive index change is feasible without apparent optical interference, specifically using methods like Talbot self-imaging and Schlieren imaging.⁸⁹ Initially, time-resolved refractive index images were captured through Schlieren imaging, a technique where part of the illumination light undergoes a phase shift to convert the phase image into an amplitude image. This method was

successfully applied to observe millisecond dynamics in photo-responsive liquid crystals.⁸⁸ However, in our research,²⁵ we discovered that the image quality achieved with Talbot self-imaging matched that of Schlieren imaging. In Talbot self-imaging, the image is slightly defocused by a few microns to transition the phase image into an amplitude image, yielding a spatial resolution of about $3\ \mu\text{m}$ in our optical setup. We optimized refractive index imaging by enhancing the responses from both acoustic and thermal gratings when using the stripe pattern of pump illumination, as detailed in our work.²⁵ The refractive index change, primarily induced by changes in density from acoustic waves and temperature variations, is maximized for observation.

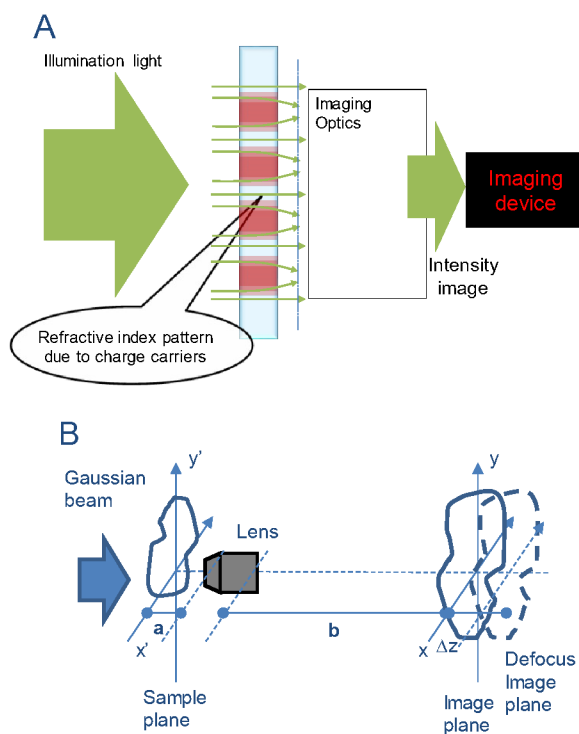


Figure 3 **A.** Schematic drawing of the principle of the PI-PM imaging technique. **B.** The drawing of the image calculation is shown. A Gaussian beam is illuminated to a phase object, and the image is calculated at the image plane and the defocused planes. Reproduced from ref. 25,90 with permission from American Institute of Physics, copyright 2019, 2021..

Despite the optimized conditions for refractive index imaging, the inherent inclusion of the TA response is unavoidable, as the optical setup for our measurements closely resembles that used in the transient absorption method. However, we managed to circumvent the influence of the TA signal by carefully choosing the wavelength of the probe light.⁹¹ At this selected wavelength, the transient absorption signal was deemed insignificant in our research. Further validation of this approach was

achieved by aligning the focus position to a focus point where only the transient absorption change is observed. Nevertheless, the TA signal response was found to be negligible.

During PI-PM imaging, a defocusing technique is employed. Throughout various experiments, we observed an improvement in the sensitivity of phase-contrast images when the focus was adjusted to an ideal defocused state. This focus modification makes the method suitable not only for smooth film surfaces but also for rough or unclean ones, offering a notable advantage over TA microscopy, especially in the context of photocatalytic material applications. The enhancement in phase sensitivity through defocused adjustment was corroborated by wave optics theories applied to a model rough film surface. This theoretical prediction was subsequently validated using particulate TiO₂ samples.

It should be remembered that there are two types of refractive index changes; one is the patterned refractive index pattern induced by the pump light, and the other is the refractive index change due to sample inhomogeneity even under the uniform illumination. In both cases, the refractive index change is simply imaged with an imaging microscope using the defocusing method. In the following, the enhancement of the refractive index image on a model surface with inhomogeneity under the uniform illumination is explained. We hypothesized that imaging a rough surface with a random structure through a lens onto the camera plane would look like what is depicted in Figure 3B. Our investigation focused on how film surface roughness amplitude and defocus distance impact the image. In our actual experiments, a sample was imaged using an objective lens followed by an imaging lens. However, for a simplified understanding, we considered the use of just a single lens to project the sample's image onto the image plane. We modeled the sample surface as having a random structure, characterized by specific values for correlation length and average structural height, and assumed the material to be composed entirely of a pure phase object. A Gaussian beam was directed at this structured film surface. The light then travels a distance 'a', passes through the lens, and continues for a distance 'b' before forming an image on the image plane.

In the wave optics,⁹² the phase profile, $\Psi_p(x,y,z)$ following propagation over a distance z is described as,

$$\Psi_p(x,y,z) = \exp(-jk_0z) \left(j \frac{k_0}{2\pi z} \right) \exp \left(-j \frac{k_0}{2z} (x^2 + y^2) \right) \times \iint \Psi_{p0}(x',y') \exp \left(j \frac{k_0}{z} (xx' + yy') \right) dx' dy' \quad (1)$$

, where $\Psi_{p0}(x',y')$ represents the object's phase profile and k_0 is the wavevector. This calculation is simplified when conducted in the Fourier domain on the xy plane, as,

$$\Psi_p(k_x, k_y, z) = \Psi_{p0}(k_x, k_y) \exp(-jk_0z) \exp \left(-j \frac{2z}{2k_0} (k_x^2 + k_y^2) \right) \quad (2)$$

, where k_x and k_y denote the spatial wavevectors in the xy plane. Additionally, the transmission through a lens with a focal length f is characterized as,

$$\Psi_p(x,y,z) = \Psi_{p0}(x',y') \exp\left(j\frac{k_0}{2f}(x^2 + y^2)\right) \quad (3)$$

The propagation over distance 'a', followed by the lens's transmittance and further propagation 'b', can neutralize the quadratic phase terms in Equations (2) and (3), $\exp\left(-j\frac{k_0}{2a}(x^2 + y^2)\right)$, $\exp\left(j\frac{k_0}{2f}(x^2 + y^2)\right)$ and $\exp\left(-j\frac{k_0}{2b}(x^2 + y^2)\right)$ at the image plane due to the relation of $\frac{1}{f} = \frac{1}{a} + \frac{1}{b}$. Consequently, the original image, $\Psi_{p0}(x',y')$ is reproduced at the image plane, albeit scaled by a factor of b/a. In cases where the sample is a pure phase object, no amplitude image is formed at the focal plane.

Under defocused conditions, the phase image undergoes further propagation, and as a result, the quadratic phase is not nullified. In Equation (2), the quadratic phase term from additional propagation, $\exp\left(-j\frac{2\Delta z}{2k_0}(k_x^2 + k_y^2)\right)$, combines with the image's pure phase distribution, $\Psi_{p0}(k_x, k_y)$ to generate an amplitude image. Typically, structural details can be obscured due to diffraction in such additional propagation. However, a minor extent of propagation can transform the phase profile back into an amplitude image. (In cases where the phase structure is periodic, the structure is fully restored, a phenomenon known as Talbot self-imaging.⁸⁹) By applying Equation (2), we were able to capture images at defocused positions that included this extra propagation.

In our simulation, the phase object, $\Psi_{p0}(x',y')$ undergoes a Fourier transformation to $\Psi_{p0}(k_x, k_y)$. This is followed by applying operator calculations for propagation to the lens, lens transmission, propagation to the image plane, and a slight additional propagation. The image intensity is then determined through an inverse Fourier transform. To comprehend the impact of photo-induced refractive index changes, the refractive index of the phase object was altered by 1%, and the entire calculation process was repeated. We compared the differences in image intensities before and after this refractive index change by subtracting the two sets of images. This comparison took place both at the image plane and at planes with added propagation distances.

The process of transforming a phase image into an amplitude image by defocusing was analyzed through optical simulation. This was done to verify the amplitude image of a textured surface using defocusing. The lens's focal length was fixed at 10 mm, and the distances from the image to the lens and from the lens to the image plane were set at 12.5 mm and 50 mm, respectively. This setup was to meet the lens equation $(1/a) + (1/b) = (1/f)$. A coherent Gaussian beam, with a 0.5 mm diameter, served as the illuminating (probe) light in a collimated state for the specimen. Figure 3B presents the simulation's schematic design. A phase object with random roughness was created, having an average roughness of 0.2 μm and a roughness correlation length of 0.05 μm .

Figure 4 illustrates various aspects: the film surface structure in Figure 4A, the initial condition

of the Gaussian beam in Figure 4B, and the intensity profile at the image plane in Figure 4C. Since the structure involves phase variations, the amplitude images at both the input and image planes display pure Gaussian profiles. A minor defocusing allows for the reconstruction of the film surface structure, as shown by comparing, following the principles outlined in the theory section. The initial pure phase profile of, $\Psi_{p0}(x',y')$ transforms into an amplitude image with an additional propagation, represented by the expression $\exp\left(-j\frac{2\Delta z}{2k_0}(k_x^2 + k_y^2)\right)$. This signifies that film surface roughness can be transformed into an amplitude image through defocusing. In this scenario, the ideal defocusing length was found to be 6 mm. The perfect defocusing distance needed for a distinct image of the film surface structure is influenced by the average roughness; as the roughness increases, the required defocusing distance decreases.

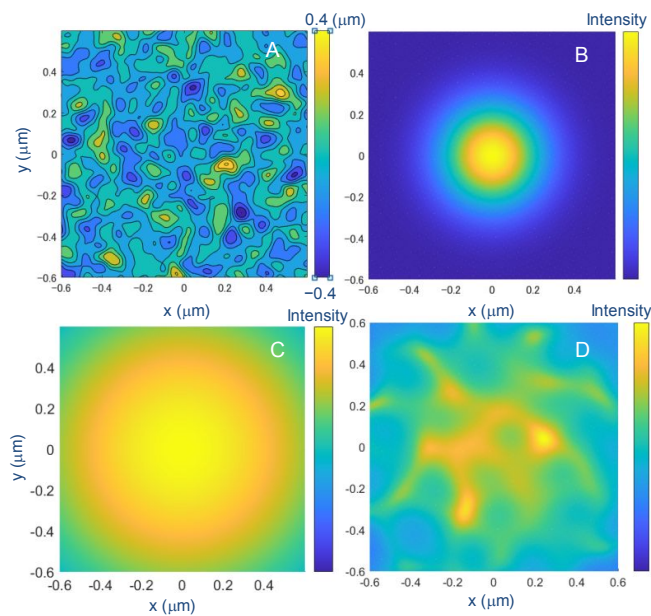


Figure 4 **A.** The assumption of the random film surface structure is shown as a film surface roughness profile, **B.** The beam intensity profile at the input plane with a Gaussian profile, **C.** the intensity profile at the image plane at the focus position, and **D.** the intensity profile at the defocused position ($\Delta z = 6$ mm) are shown as the light intensity profile. Reproduced from ref. 90 with permission from American Institute of Physics, copyright 2021.

Subsequently, the variation in image brightness due to a minor change in refractive index was assessed at both the image plane and a suitably defocused distance. Figure 5 displays the differential image, captured before and after a 1% alteration in the refractive index, alongside the original images

at both the in-focus and defocused locations. The image reflecting the refractive index alteration was noticeably more pronounced at the defocused spot compared to the image plane. To evaluate the enhanced sensitivity to refractive index changes, the average standard deviations of pixel intensities across the images were calculated. The sensitivity was found to be 30 times greater at the defocused position than at the focused position. This suggests that phase-contrast imaging can be significantly enhanced with optimal defocusing.

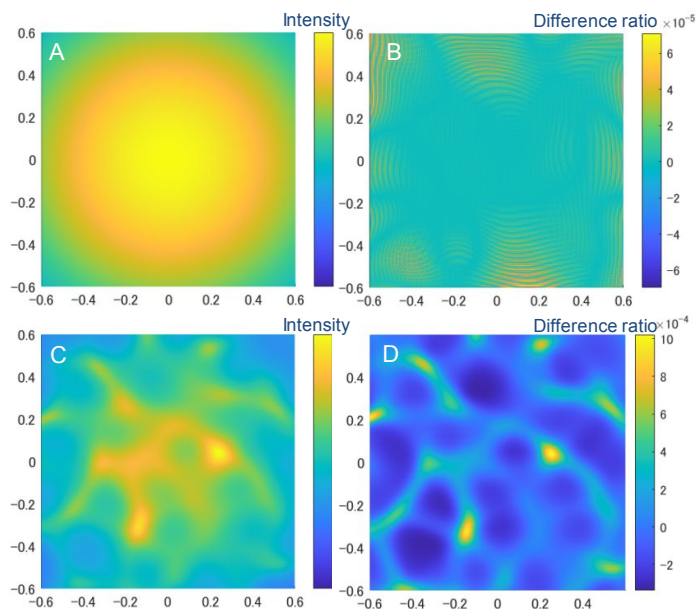
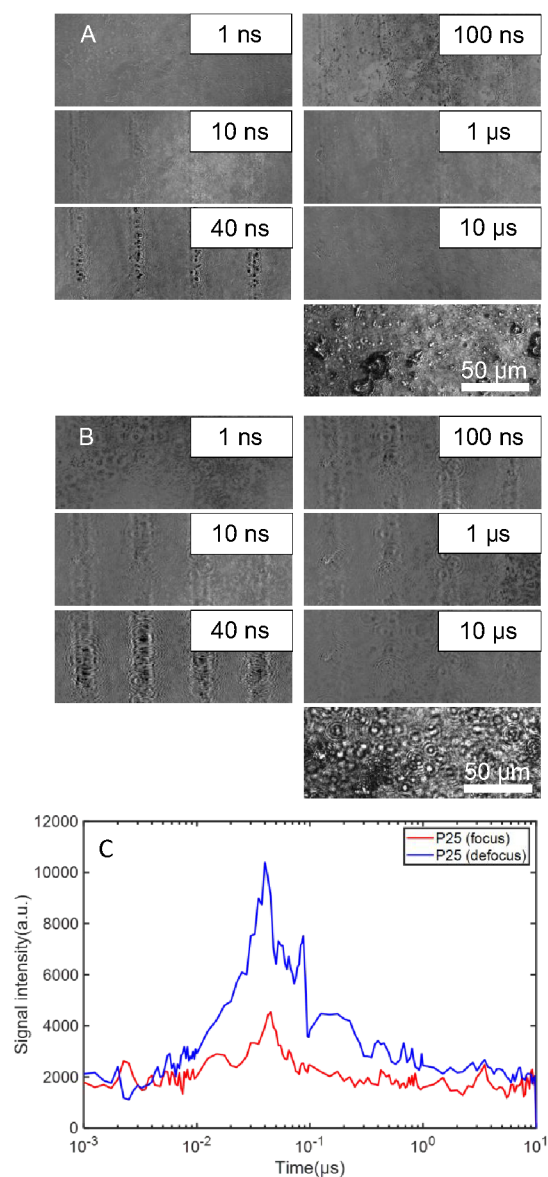


Figure 5 The subtraction images before and after the refractive index change ($\Delta n = 0.01$) were investigated at the image plane and the optimal defocused position. **A, C**. The light intensities of the original images at the image plane and at the optimal defocus position and **B, D**. the difference ratio of the light intensity of the subtraction images before and after the refractive index change are shown, respectively. Reproduced from ref. 90 with permission from American Institute of Physics, copyright 2021.

For demonstration purposes, substrates composed of P25 particles, which contained many aggregates and particles in the micron range (with 50-200 nm particles observable in SEM images), were utilized. The roughness of these P25 substrates was measured at 700 nm. This was contrasted with a flat surface made from PST-18NR paste (anatase structure, JGC Catalysts and Chemicals). To test the enhancement of subtraction images caused by refractive index changes under defocused conditions, TiO_2 substrates were examined at both the image plane and defocused positions. Figure 6 displays the PI-PM image sequence for a P25 substrate at each position, alongside the original optical images taken under the same setup. The ideal signal condition was determined by adjusting the focus

until the image contrast, influenced by patterned light illumination, was at its maximum. While the original optical image at the bottom of Figure 6B appeared blurry due to defocusing, the contrast resulting from the refractive index change was more pronounced than in the focused condition. The stripe's amplitude was determined by performing a Fourier transform horizontally across the image, with the Fourier amplitude depicted in Figure 6C. The refractive index amplitude was enhanced fivefold under defocused conditions compared to focused conditions. During the actual experiment, the position of the objective lens was adjusted for alignment stability.

Figure 6 The PI-PM image sequences under **A** the focus and **B** the defocus conditions are shown for a P25 substrate. The bottom images in **A** and **B** corresponds to the original optical images, and the PI-PM images were obtained by subtracting the original images from the photo-excited images. **C**



corresponds to the temporal change of the stripe amplitudes for each image sequence, corresponding to the photo-induced refractive index change. Reproduced from ref. 90 with permission from American Institute of Physics, copyright 2021..

In the case of this sample, the image contrast heightened significantly within 50 to 80 ns and then diminished in less than 1 microsecond, exhibiting a slight, slower decay. These dynamics are indicative of carrier trapping and recombination processes. For a P25 substrate, the thermal response was considerably less pronounced. This can be attributed to the inefficiency in thermal generation and heating of the film in particle-based samples, owing to the restricted propagation of charge carriers or phonons beyond the individual particles.

In this work, we present a theoretical framework explaining how photo-excited charge carriers on rough film surfaces can be detected using the PI-PM technique. When capturing phase-contrast images, the phase variations caused by rough film surfaces can be integrated with the quadratic phase term through defocusing. This integration enhances the sensitivity to phase changes resulting from photo-excited charge carriers. This phenomenon can be modeled using wave optics theory. The increase in the effectiveness of PI-PM images through defocusing was demonstrated. These findings affirm the effectiveness of the PI-PM method for examining samples with rough film surfaces and provide insights into the behavior of photo-excited charge carriers in particulate photocatalytic materials.

2.3 Image recovery by the informatics calculations

The image recovery calculations are the key for the PI-PM method. You may feel that the local analysis described in section 2.4 and many examples in 3 do not need the pattern-illumination of the pump light. However, it is necessary to apply all the image recovery calculations because they use the contrast between the illuminated and non-illuminated regions. Without these image recovery calculations, the following local analyses under the light illuminated regions is impossible. Thus, the combination of the pattern-illumination and the image recovery calculations are prerequisite. The paragraph describes the use of three distinct methods for image enhancement or correction, based on the image's quality. These methods include: 1) flat field correction, 2) image reconstruction using robust principal component analysis, 3) three-dimensional total variation regularization.

In the process of flat field correction, the issue of image flickering, a common occurrence with pulse-light illumination due to inherent pulse intensity variations and uneven spot intensity, was addressed. This was resolved by subtracting the background intensity using a mean-value filter, which incorporated a kernel function defined by the user. This image processing technique effectively homogenized the background intensities and standardized the intensities in the areas of excitation.⁸⁵

The second image processing technique involves eliminating random patterns or noise by assessing the sparsity structure in each image, a common approach in image reconstruction. In this method, the image data is treated as a matrix A , with dimensions $M \times N$ (200 x 1024 pixels). The process retains the r -th largest principal component analysis (PCA) components in the matrix following a specific calculation.^{93–95}

$$\text{Minimize}_{A, L \in \mathbb{R}^{M \times N}} \|A - L\|_F \text{ subject to } \text{rank}(L) \leq r$$

where F indicates the Frobenius norm of the matrix, and L is an image matrix consisting of the principal components with the same size as A .

This method involves a calculation where the discrepancy between the original image, denoted as A , and its low-rank counterpart, L , is measured using the Frobenius norm. However, this approach often fails in the presence of outlier values. In robust PCA (RPCA), the low-rank matrix and the error matrix are defined by a specific equation.

$$\text{Minimize}_{L, S \in \mathbb{R}^{N \times M}} \|L\|_* + \lambda \|S\|_1 \text{ subject to } A = L + S$$

where S is the sparsity matrix of the image corresponding to the noise matrix, and $*$ indicates the nuclear norm of the matrix.

The image data contains various numerical patterns, viewed as components within the data, and these are classified using principal components found in the image data. This data is broken down using singular value decomposition into a $U \cdot T \cdot V$ matrix configuration, where T represents the eigenvalue matrix, U the vertical line matrix, and V the horizontal line matrix. The image is perceived as a synthesis of the outer products of U 's vertical line vectors and V 's horizontal line vectors. Through this process, the principal components and sparse noise elements within the image are progressively distinguished. This technique divides the random patterns caused by errors into a sparsity matrix, while preserving the principal structure with the least number of elements.

Our findings indicate that RPCA is effective in distinguishing between structured patterns and coherent noise patterns, even in the absence of prior information. An illustrative example of this is presented in Figure 7. In the coherent imaging process, a laser is used to illuminate a sample, often leading to the observation of ring patterns caused by dust or other elements in the optical path. These create a specific kind of light diffraction known as a coherent moiré pattern. In the original PI-PM image, these coherent moiré patterns were identified and isolated through this method, allowing for their removal.

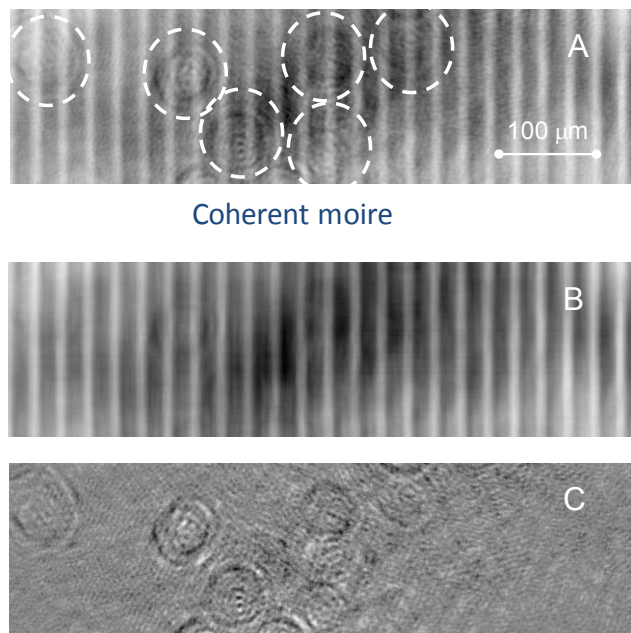


Figure 7 An example of the image recovery application of the robust principal component analysis (RPCA) method. The sample was a TiO_2 film measured by the PI-PM method at $t = 1 \mu\text{s}$. **A**: An original signal image was processed by the RPCA method, and **B**: the low-rank image was separated from **C**: the sparse image clearly. Reproduced from ref. 85 with permission from American Institute of Physics, copyright 2020.

Finally, we will introduce one of the most effective image recovery methods for PI-PM image sequences; three-dimensional total variation regularization (3DTV) method. The optimized equation is shown here.

$$\underset{A \in \mathcal{R}^{N \times M \times K}}{\text{Minimize}} \left(\frac{1}{2} \left\| A_{\text{true}} - A \right\|_2^2 + \lambda_1 \sum_k \lambda_2 \sum_j \sum_i \left| \text{diff}(A_{i,j,k}) \right| \right)$$

, where A_{true} is the true image sequence and A is the measured image sequence, and the second term corresponds to the differential term for the regularization. In this calculation, the squared sum of the true and measured data was minimized with a differential regularization term. The regularization term has two hyperparameters, λ_1 and λ_2 , because they need to be optimized for the spatial and temporal dimensions.

One of the examples for a Fe_2O_3 photoanode is shown in Figure 8. Before the image recovery, the image contrast of the signal was too weak to observe any features, but after the noise reduction and smoothing effect by the 3DTV, the time sequence was clearly recovered.

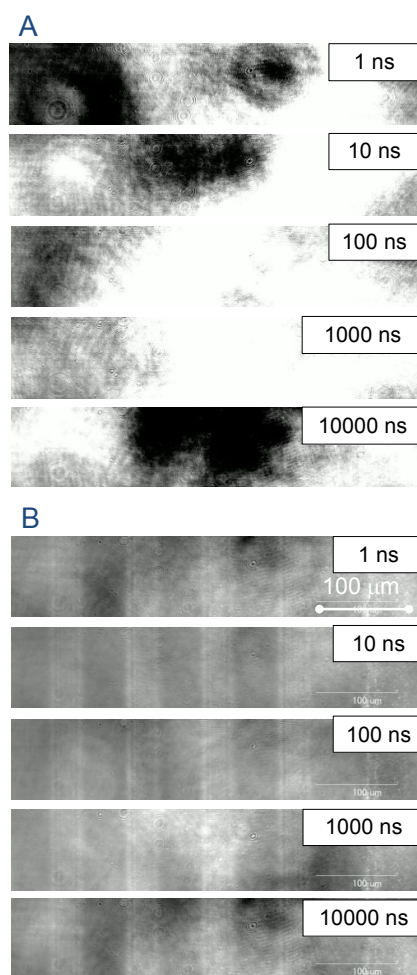


Figure 8 An example of the image recovery application of the 3D total variation (3DTV) regularization method. The sample was a Fe_2O_3 film measured by the PI-PM method until 10000 ns. **A**: An original signal image was processed by the 3DTV method, and **B**: image sequence was recovered.

2.4 Charge carrier type mapping using the clustering responses

In the PI-PM approach, clustering analysis plays a key role in discerning the behavior of charge

carriers locally within the measurement region. This methodology serves two primary purposes: uncovering minor hidden reactions and identifying the types of charge carriers. To illustrate the initial challenge, consider the example shown in Figure 9. This figure presents a series of images sequence changes in the refractive index of a nanoparticulate-TiO₂ film contacting with ACN. The time frame ranges from nanoseconds to microseconds. It also includes a diagram at the bottom showcasing the pattern of the pump light. Areas under the light illumination displayed noticeable differences due to the generation of photo-excited charge carriers. These illuminated regions slowly faded over an estimated 10 μ s. Consequently, the overall refractive index alteration diminished, primarily because of the recombination of charges. Moreover, several bright spots appeared and disappeared, mostly within the initial 50 ns.

At first, the collective response was examined by computing the mean pixel intensity for each image, both horizontally (X) and vertically (Y). Figure 9B depicts the average transient response extracted from Figure 9 Post pulse exposure, the mean signal surged quickly and then gradually reduced over an estimated period of 10 \pm 5 μ s. This decline corresponds with earlier observations of refractive index variations in nanoparticulate TiO₂ films, which ascribe the reduction due to the recombination of diverse charge carriers, like electrons and holes, across various trapping states. The detected response exhibited a non-linear decay ranging several time scales, indicating a mix of distinct recombination mechanisms. Importantly, the transient bright spots noticed around 50 ns were not evident in this averaged response, as they were eclipsed by the more prevalent average responses.

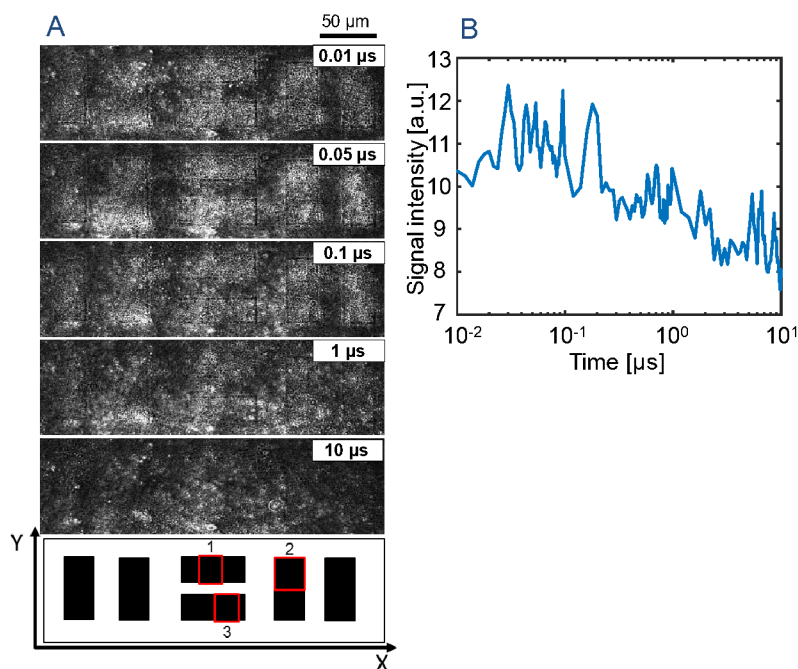


Figure 9 A. An image sequence of the refractive index change for a nanoparticulate TiO₂ (P25)

film/acetonitrile on the order from nanoseconds to microseconds. The light intensity pattern of the pump light is indicated at the bottom of the figure, and the selected regions for the cluster analysis were indicated in red squares. The scale bar corresponds to 50 μm . **B**. The averaged response of the refractive index change obtained from the image sequence of **A**, which was obtained by averaging the brightness (amplitude) in the images in X and Y direction. Reproduced from ref. 86 with permission from American Institute of Physics, copyright 2020.

To discern the rare local responses, we utilized clustering analysis to sort the responses of charge carriers. Normally, responses of charge carriers are modeled with multi-exponential functions. Yet, for nanoparticulate films, this method is often inadequate as the responses typically vary from exponential functions, influenced by diverse decay mechanisms. To overcome this, we implemented a technique to directly categorize transient responses based on their shape similarity (cluster analysis). Figure 10 illustrates this process. We initiated by selecting a square irradiation area from Figure 9 and gathered local responses from the image sequence. These responses were then classified into groups based on the resemblance of the decay profiles. This approach circumvents the assumption that the decay response follows a parametric form, like a combination of exponential functions. We chose spectral clustering, favored for its uncomplicated execution. The classification of responses into categories was achieved through experimentation, resulting in three distinct groups, with anomalies excluded from these groups.

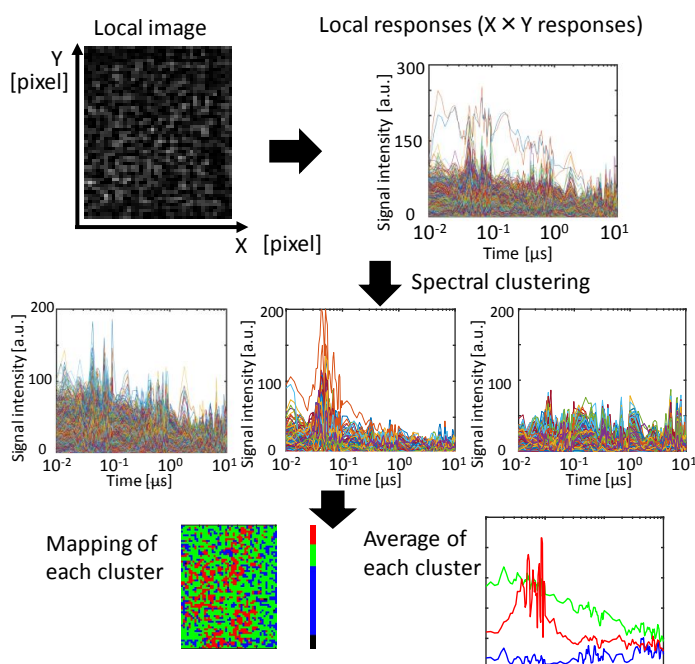


Figure 10 Schematic of the clustering analysis. Local responses were extracted from image sequence obtained by phase microscope, and the responses were classified into some categories according to the data similarity (rate and intensity). In this example, the responses were classified into three categories. After this process, the responses of each category are averaged, and also each category is mapped in color on the original surface. Reproduced from ref. 86 with permission from American Chemical Society, copyright 2020.

Figure 11 presents a sample analysis of a nanoparticulate TiO_2 film. A specific region with 20 x 30 micrometers was chosen for this analysis. Following this, 150,000 transient responses from local pixels were examined using clustering techniques. These responses were divided into three distinct categories, each represented by a different color on a map. Additionally, the average transient responses corresponding to each category were displayed. It's clear that there are three kinds of responses: a slow response, a spike response, and no response at all. (The origin of the responses are described in section 3.3.) Typically, these different response types are obscured when all the response data is averaged.

It was expected that the charge carrier dynamics can be affected by the neighboring sites (pixels), and the charge carrier diffusion should be observed by the inter-communication between the neighboring pixels. Although we could recognize it for the thermal diffusion (recognized in Figure 2), we have scarcely observed the inter-communication between pixels for the charge carrier dynamics. However, we suppose that this is due to the sample conditions of photocatalytic materials; they mostly consist of particles. The charge carrier transport for these materials occur via the hopping of the states. Since the transport process is too slow or less frequent to observe under our experimental setup, we could not detect the inter-pixel communication is negligible for an optical resolution of 2 μm .

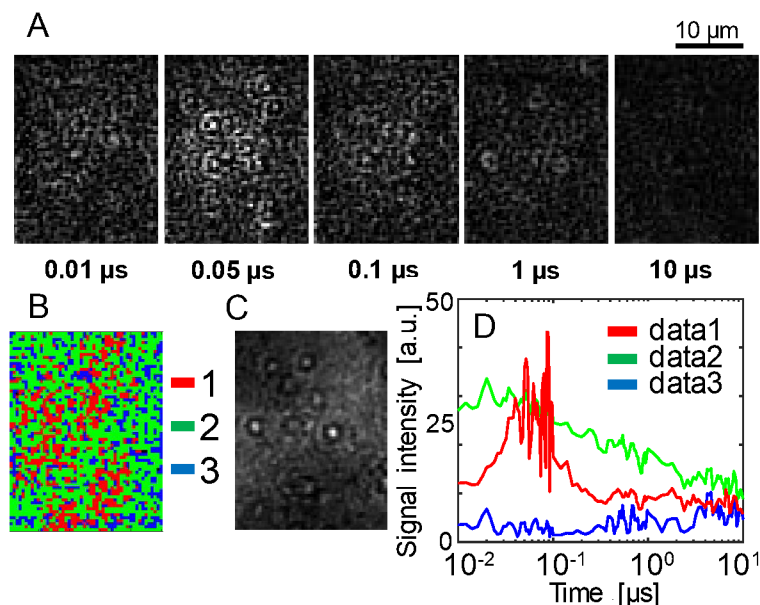


Figure 11 **A**: Image sequence of the refractive index response in a small region ($25 \times 20 \mu\text{m}^2$) on the order from nanoseconds to microseconds. The scale bar corresponds to $10 \mu\text{m}$. **B**: Categorized mapping of the charge carrier responses of **A**. **C**: Microscopic image at the same area as in **A**. **D**: Averaged responses for the categorized responses. Reproduced from ref. 86 with permission from American Chemical Society, copyright 2020.

Another benefit of clustering is its ability to identify different types of charge carriers. In time-resolved measurements like TA and TPSC, determining the types of charge carriers, including distinguishing electrons and holes as well as trapped carriers is challenging. However, the map of charge carrier types generated from clustering analysis offers a distinct separation of regions with different charge types. This distinction becomes more apparent when combined with the effect of scavengers, facilitating easier identification of the types of charge carriers.

Take, for instance, the analysis of a BiVO_4 particulate film (as shown in Figure 12). We selected regions of 40×40 micrometers within the illuminated area for this purpose. By analyzing the time sequence of images captured using the PI-PM method, we extracted time responses from all pixels, categorizing local responses based on signal shape similarity. In acetonitrile, we identified three types of responses: faster, slower, and no responses, and prepared a categorized map for these.

When we repeated the experiment in ethanol, a common hole scavenger, we observed similar response types. However, the categorized map revealed noticeable differences. The dispersed red regions, indicative of a specific response type, diminished with the addition of ethanol (except around the edges of black regions, corresponding to particle aggregates). This change suggests that the red response is related to hole response, as it is scavenged by the hole scavenger. By using similar processes with different scavengers, we were able to distinguish between various types of charge carriers. Generally, different responses in time-resolved measurements may overlap or cancel each other out, but by analyzing responses based on measurement position and visualizing the effects of scavengers through mapping, these responses can be effectively separated and identified. Although the effect of the scavengers has been seen in the change in the response shape in most of the previous studies, we figured out that the response shape is changed because they are averaged in all the regions, and actually the ratios of different charge carrier types are changed, revealed by the clustering analyses, which are revealed in several examples for photocatalytic materials.

For most of the materials, the probe wavelength, 532 nm is located in the longer wavelength region than the band gap absorption. Under this condition, the dielectric function is described by the Drude theory, where the dielectric property is determined by the induced polarization of charge carriers, represented by the Lorentz model. In this case, the susceptibility (χ), which has the relation with the permittivity ($\epsilon = \chi + 1$), as

$$\chi(\omega) = -\frac{Ne^2}{m\epsilon_0 i\omega\gamma - \omega^2}$$

, where N is the number of charges, m is the charge mass, ϵ_0 is the vacuum permittivity, γ is the damping parameter and ω is the angular frequency. This is the case when electrons are considered as the charge in the Lorentz model, and $\chi(\omega)$ changes its sign for the hole charge because the applied force direction becomes opposite in the Lorentz model, as long as the material atmospheric condition is same.

When charge carriers are photo-excited, the number of charge carriers, N is changed, and the susceptibility is varied. Obviously the susceptibility change is proportional to the permittivity change. Since the permittivity is proportional to the square of the refractive index, the refractive index change is provided as,

$$\Delta n \cong \frac{\Delta\epsilon}{2n}$$

, when the permittivity change is assumed to be small. This equation tells us that the refractive index change for photo-excited electrons and holes are opposite under the same material atmosphere. This is helpful to understand the assignment of the charge carrier type, because once one of the response is assigned as electrons/holes, this indicates that the response with the opposite sign corresponds to the other type of the charge carriers.

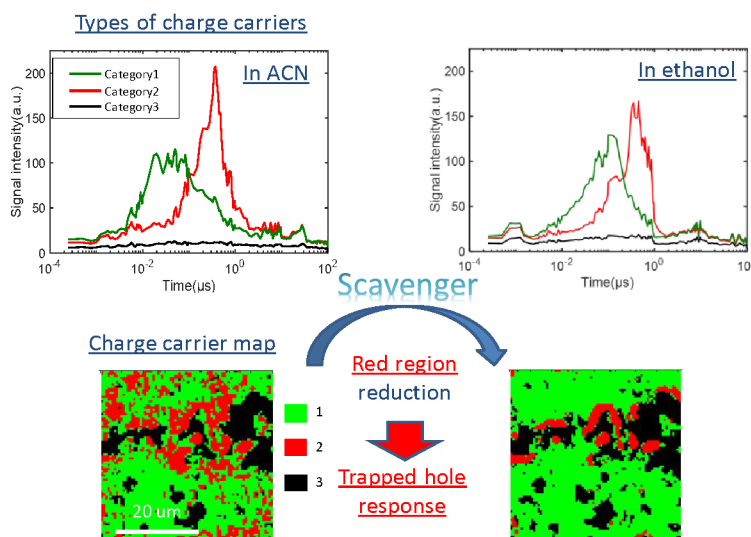


Figure 12 The method for distinction of different charge carrier types is shown using scavenger solutions. Here is an example for a BiVO_4 film. The responses for Categories 1-3 were recognized in ACN and Ethanol; however, the charge carrier mapping indicates that the red regions were affected and reduced by the hole scavenger, suggesting it corresponds to the surface-trapped holes.

2.5 Samples

We developed a nano-particulate TiO₂ film using a titania nanoparticle paste with an anatase crystal structure (PST-18NR, JGC Catalysts and Chemicals) and a mixture of anatase and rutile (P-25). The paste was spread onto a glass slide (Matsunami Glass) through the doctor-blade technique, then sintered at 450 °C for 2 hours to remove all solvents and chemicals present in the paste. The final film consisted of TiO₂ nanoparticles, typically 10-20 nm in size.

To produce a hematite film, β-FeOOH was synthesized on a fluorine-doped tin oxide (FTO) substrate (~7 Ω/sq, SOLARONIX). This involved using a solution containing 0.15 M iron (III) chloride hexahydrate (FeCl₃ · 6H₂O, 99.9%, Wako) and 1 M sodium nitrate (NaNO₃, 99.9%, Wako) at 100°C for 1 hour. The β-FeOOH was then converted to hematite (α-Fe₂O₃) by sintering in Ar gas at 650°C for 30 minutes, creating a film about 500 nm thick.

For the perovskite film made of methylammonium lead iodide (MAPI), we prepared a precursor solution using lead iodide (PbI₂) and methylammonium iodide (MAI) in dimethylformamide (DMF) (Tokyo Kasei). This was spin-coated onto a substrate and recrystallized with diethyl ether, followed by post-annealing to form a MAPI film 500 nm thick.⁹⁶ Hole transport layers (HTLs) such as 2,2',7,7'-tetrakis-(N,N-di-4-methoxyphenylamino)-9,9'-spirobifluorene (spiro-OMeTAD), poly[bis(4-phenyl)(2,4,6-trimethylphenyl)amine] (PTAA), and poly(3-hexylthiophene-2,5-diyl) (P3HT) were applied on MAPbI₃ films. Spiro-OMeTAD (112 mg/mL), PTAA (112 mg/mL), and P3HT (54 mg/mL) in chlorobenzene solutions were deposited in 20 μL volumes onto the MAPbI₃ films. Spiro-OMeTAD and PTAA were used undoped and exhibited low charge mobility within the films. The films were then spin-coated at 4000 rpm for 20 seconds and dried by heating at 100 °C for 10 minutes.

97–99

For particulate chemicals, a paste was prepared by manually grinding particle powder and ethanol in a mortar for 1 minute, a process repeated 15 times. Ethanol, terpineol, and ethylcellulose were added and stirred manually for 10 minutes, then evaporated to remove the ethanol. This paste was applied to a glass slide using the doctor-blade method and sintered at 450 °C for two hours.

For comparison, single crystalline TiO₂ and SrTiO₃ (Furuchi Chemicals) with dimensions of 10 x 10 x 0.5 mm and a polished (110) surface were utilized.

To assemble a solid/liquid cell, another glass slide was placed with a silicon rubber spacer (0.5 mm thick). A liquid layer on the film was created by sandwiching another glass slide with a silicon rubber spacer (0.5 mm thick). Acetonitrile (ACN), ethanol (EtOH), and 0.1 mM nitrobenzene (NB)/EtOH were introduced into the gap. ACN acted as an inert liquid phase to prevent charge transfer from TiO₂ to the liquid, which would lead to rapid scavenging of photo-excited electrons by oxygen in air or water. EtOH served as a typical hole scavenger, and NB/EtOH was used as a scavenger for both electrons and holes.¹⁰⁰

3. Results and discussions

3.1 Lifetime homogeneity of a nanoparticulate film ²⁵

In the early times of the development, we measured the PI-PM image sequence at the defocus point, where the signal's amplitude was maximized at the expense of spatial resolution. Using the ideal signal intensity conditions, we captured a series of PI-PM images of a nanoparticulate (NP)-TiO₂ film in contact with ACN, ranging from nanoseconds to milliseconds, as shown in Figure 13. In these images, the bright areas in the striped pattern indicate the excited region illuminated by the pump light, where the photo-excited carriers are generated. The emergence of the stripe pattern is due to the change in the refractive index, which occurs because of the generation of photo-excited carriers and the subsequent temperature increase from their decay. These bright areas progressively intensify up to 1 μ s, begin to diminish over approximately 100 μ s, and completely fade on the millisecond scale. This observation demonstrates that both the relaxation processes of the photo-excited carriers and their thermal decay can be effectively monitored using the PI-PM imaging technique.

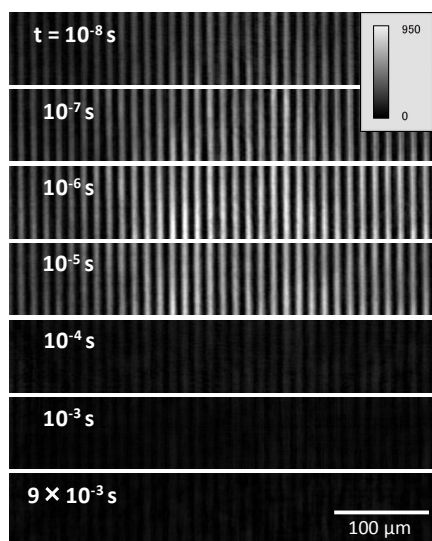


Figure 13 A PI-PM image sequence for a nanoparticulate TiO₂ film / acetonitrile from the nanosecond to millisecond order. The scale bar corresponds to 100 μ m. Reproduced from ref. 25 with permission from American Institute of Physics, copyright 2019.

In order to interpret the response, we analyzed the temporal change in amplitude at the spatial frequency corresponding to the reciprocal of the grating spacing. This was achieved through Fourier transform of the periodic stripe pattern along the x-direction, as indicated in Figure 14. Figure 14A

illustrates the calculation method and provides examples of Fourier spectra for the spatial frequency. The amplitude of the diffraction order represents the collective dynamics of the photo-excited carriers and subsequent thermal diffusion across the entire image area. This information is largely consistent with that obtained from the conventional transient grating (TG) response. The signal intensity initially rises with oscillation for several microseconds, then decays over a period of about 100 μs . The early oscillatory response, detailed in the inset of Figure 14B, is attributed to the acoustic grating.⁶¹ This indicates that an acoustic wave is produced due to the periodic pattern of thermal expansion, which in turn causes oscillations in the refractive index via density modulation. The acoustic wave's velocity was determined to be 1.3×10^3 m/s, calculated using the formula $c = \lambda/T$ (c : sound velocity, λ : grating spacing, T : oscillation interval). This velocity aligns more closely with that of acetonitrile (1290 m/s) rather than TiO_2 (~ 7000 m/s), a discrepancy that is not yet fully understood.¹⁰¹ The increasing response up to 1 μs corresponds to the decay of photo-excited electrons to lower energy states.^{35,61} The decay phase lasting until 100 μs is primarily due to thermal diffusion in the TiO_2/ACN system, a characteristic also observed in conventional TG methods. The fact that the average dynamics of the PI-PM imaging response agrees with those of the conventional TG response lends credibility to the PI-PM imaging data for measuring charge carrier dynamics.

Sometimes it is difficult to separate the thermal and charge carrier responses. The thermal effect can be observed usually later than the charge carrier dynamics, extending typically to hundreds of microseconds, depending on the materials' thermal properties. Thermal diffusion can be recognized in Figure 2 by smearing out the photo-illuminated region. In the nanosecond to microsecond range, we can usually ignore the thermal response. The other important experimental confirmation is that the charge carrier responses can be scavenged by the scavengers described in Section 2.2 and 3.4. Since the thermal response is not affected by the scavenger species, we can recognize the thermal response. Based on these two facts, we can distinguish the thermal response from the charge carrier response.

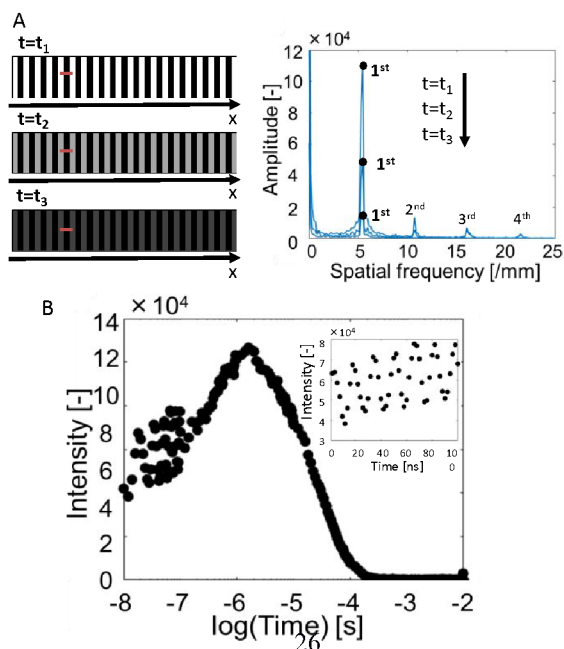


Figure 14 **A**: A schematic drawing of the calculation procedure to obtain an amplitude of the average refractive index change is shown. For an image at each delay time, the Fourier transform was calculated in the x direction, and the first order amplitude of the Fourier spectrum was regarded as the average amplitude of the refractive index change. **B**: A temporal change of the amplitude of the PIM images. The temporal change of the amplitude at the 1st order of spatial frequency was plotted. The inset shows the oscillating response on the nanosecond time scale, corresponding to the response of the acoustic grating. Reproduced from ref. 25 with permission from American Institute of Physics, copyright 2019..

We observed various responses, including the oscillatory behavior from the acoustic grating, the decline of electrons trapped on the surface (up to 1 μ s), and thermal diffusion (lasting up to 100 μ s). To capture the lifetimes of the photo-excited electrons, we focused on a specific time frame (0-1 μ s) for the response. This segment was modeled using an exponential function, allowing us to map out the time constants. Our findings revealed a broad distribution of these time constants, ranging from 68 to 920 nanoseconds, which varied depending on the locations within the sample. This significant variation implies that the uniformity of the sample plays a crucial role in determining the lifetimes of the charge carriers.

3.2 Charge carrier diffusion in nanoparticulate films ¹⁰²

Understanding the dynamics of charge carriers has been challenging due to two main issues: the disparity between single crystals and particulate films, and the different assignment yielded by different methods. Focusing on the first issue, the dynamics of charge carriers in single crystalline TiO₂ and SrTiO₃ were characterized by a single exponential decay, which immediately followed irradiation by the pump pulse.^{33,54} In contrast, particulate films exhibited varied charge responses. For particulate films of TiO₂ and SrTiO₃, it is believed that photo-excited charge carriers typically became trapped within 100 ps, with the trapped carriers decaying through recombination in the microsecond range.^{23,24}

Regarding the second issue, time-resolved absorption (TA) responses indicated several types of decay in TiO₂^{23,24} and SrTiO₃^{103–105}, with time constants ranging from under 100 ps to several microseconds. In transient photovoltage (TP) measurements, two decay types were observed in the visible and near-infrared spectrum. These were attributed to carriers trapped in shallow and deep trap states, with decay times ranging from nanoseconds to microseconds for TiO₂.^{40,106} Conversely, changes in the refractive index indicated an initial increase over hundreds of nanoseconds, followed by decay within 1-100 microseconds. Similar responses were also observed in other particulate semiconductor films like Fe₂O₃, BiVO₄, and methylammonium lead iodide (MAPI).⁸²

A notable difference in the response observed via changes in the refractive index is the

emergence of a rising component within the range of 10-1000 ns. This response cannot be attributed solely to charge trapping in defect states, which typically occurs within 100 picoseconds in other measurements. It's hypothesized that the trapping into deep, immobile states happens instantaneously, while carriers trapped more shallowly migrate between particles, resulting in a longer overall trapping process.

In light of this hypothesis, we developed a model that explains charge trapping during diffusion in the responses of TiO₂ and SrTiO₃ particulate films, as well as the observed differences between responses in single crystal and particulate films. The consistency of this model with theoretical predictions confirms that this type of trapping combined with diffusion is a common process in particulate films.

In particulate semiconductor materials, photo-excited charge carriers are typically trapped in states on the order of picoseconds. We postulate that such trapped carriers can diffuse in position and be trapped in another state during hundreds of nanoseconds. These carriers are likely trapped in shallow states, undergoing diffusion and recombination processes. The number of shallowly trapped charge carriers, denoted as N , can be represented as follows:

$$\frac{\partial N(z,t)}{\partial t} = D_N \frac{\partial^2 N}{\partial z^2} - \frac{N}{\tau}, \quad (1)$$

where D_N symbolizes the diffusion coefficient of charge carriers that are shallowly trapped, τ represents the decay time of these carriers, encompassing recombination and other forms of decay, and z denotes the direction parallel to the film's thickness. The process by which these shallowly trapped charge carriers become trapped in another state at the surface is described as follows:

$$\left. \frac{\partial N(z,t)}{\partial z} \right|_{z=0} = \frac{S}{D_N} N(0, t), \quad (2)$$

where S is the trap rate to another trap state. This model is calculated with an initial distribution of photo-excited charge carriers as,

$$N(z,0) = N_0 \exp\left(-\frac{z}{d_p}\right), \quad (3)$$

where d_p represents the apparent penetration depth of the pump light. Given that the film is composed of particles, d_p essentially reflects the ensemble-averaged depth of photo-excitation measured from the surface. The quantity of carriers that become trapped in another state is characterized as follows:

$$\frac{\partial N_{\text{trap}}}{\partial t} = S N(0, t) \quad (4)$$

The Eqs (1)-(3) can be analytically solved as,¹⁰⁷

$$N(z,t) = \frac{N_0}{2} \exp\left(-\frac{t}{\tau} - \frac{z^2}{4D_N t}\right) \left\{ W\left(\beta\sqrt{D_N t} - \frac{z}{2\sqrt{D_N t}}\right) + W\left(\beta\sqrt{D_N t} + \frac{z}{2\sqrt{D_N t}}\right) \right\} -$$

$$\frac{2\left(\frac{S}{D_N}\right)}{\left(\frac{S}{D_N}\right) - \beta} \left[W\left(\beta\sqrt{D_N t} + \frac{z}{2\sqrt{D_N t}}\right) - W\left(\frac{S}{D_N}\sqrt{D_N t} + \frac{z}{2\sqrt{D_N t}}\right) \right] \quad (5)$$

$$\text{with } W(x) = \exp(x^2) \operatorname{erfc}(x)$$

where erfc indicates the error function and $N(0, t)$, which is necessary to solve Eq. (4) to obtain $N_{\text{trap}}(t)$, is calculated as,

$$N(0, t) = \frac{N_0}{S - \beta D_N} \exp\left(-\frac{t}{\tau}\right) \left\{ -\beta D_N W(\beta\sqrt{D_N t}) + S W\left(\frac{S}{D_N}\sqrt{D_N t}\right) \right\} \quad (6)$$

Using this formula, we numerically calculated $N_{\text{trap}}(t)$. In our data analysis, we assumed the recombination of shallowly trapped charge carriers to be negligible. In other words, τ is considerably longer than the duration over which $N_{\text{trap}}(t)$ increases. The parameters S , β , and D_N were treated as variables to be determined. They were estimated by employing the Markov Chain Monte Carlo (MCMC) method, selecting values that maximized the posterior probability.¹⁰⁸

The PI-PM image sequences for both a single crystal and a particulate film of TiO_2 are depicted in Figure 15. In each sample, a striped pattern, reflecting the pattern of the pump light, was evident. This striped contrast is directly related to the change in refractive index caused by the photo-excited charge carriers and the temperature increase from nonradiative relaxation of these carriers. The stripe pattern in the single crystal exhibited a diffraction-like shape at the edges of the slit, a result of the sample's thickness (0.5 mm). The contrast of these stripes faded in the range of microseconds due to thermal diffusion, observable as a blurring of the stripe patterns. Notable differences between the single crystal and the particulate film emerged in the initial period of less than 1 μs . In the single crystal sample, the refractive index change was immediate following the pump pulse irradiation. Conversely, in the particulate film, the contrast grew more slowly, taking up to 1 μs to fully develop.

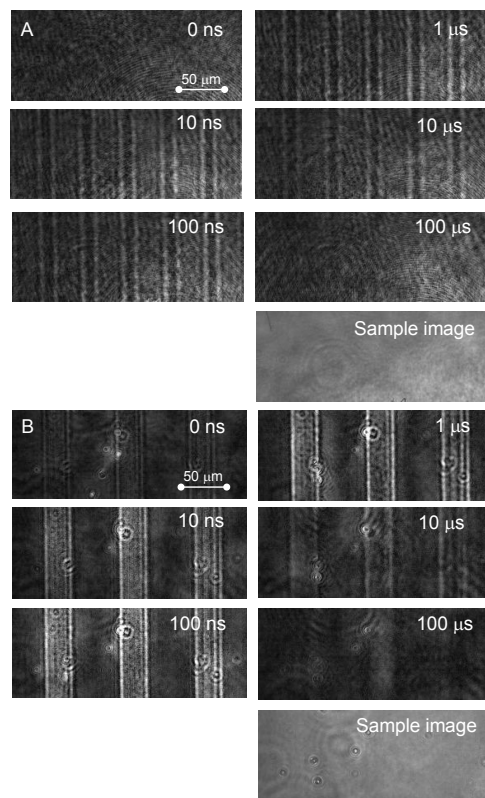


Figure 15 The PI-PM image sequences for **A**: a single crystal and **B**: a particulate TiO₂ film are shown. The optical images of the samples obtained under the same optical setup are also shown at the bottom of the sequences. Reproduced from ref. 102 with permission from MDPI, copyright 2021.

Figure 16 illustrates the temporal changes in the refractive index to clearly demonstrate the difference of the time responses. The amplitude of the stripes was determined by calculating the amplitude of the Fourier transform of each image in the horizontal direction. It was evident that the signal in the single crystal surged immediately following the pump light irradiation and exhibited a gradual decay until approximately 100 ns, followed by a decay with a time constant of around 600 ns. For the particulate film, however, the signal rose gradually until about 1 μs before decaying on the microsecond scale. This decay aligns with previously reported thermal diffusion, which occurs an order of magnitude faster in the single crystal compared to the particulate film.²⁵ A key point to note is the difference in the initial rise of the signals; in the particulate film, the signal continued to increase until around 1 μs, whereas in the single crystal, the signal declined immediately after a brief surge caused by the pump pulse irradiation.

Prior studies have indicated that in TiO₂ particulate films, photo-excited charge carriers typically get trapped in less than 100 ps and their recombination occurs over a range from nanoseconds to microseconds. In the case of the single crystal, the signal was observed to rise within our time

resolution of 3 ns and then decay with a time constant of approximately 600 ns, aligning with reported values.³³ On the other hand, the signal in the particulate film showed a gradual increase over a period of about 1 μs , a phenomenon not widely reported by other methods. This time frame is roughly the interval between the initial trapping of charge carriers in shallow states and their eventual recombination. This observation leads to the hypothesis that these carriers may be in a transitional state that permits their diffusion among particles while they are in these shallowly trapped states.

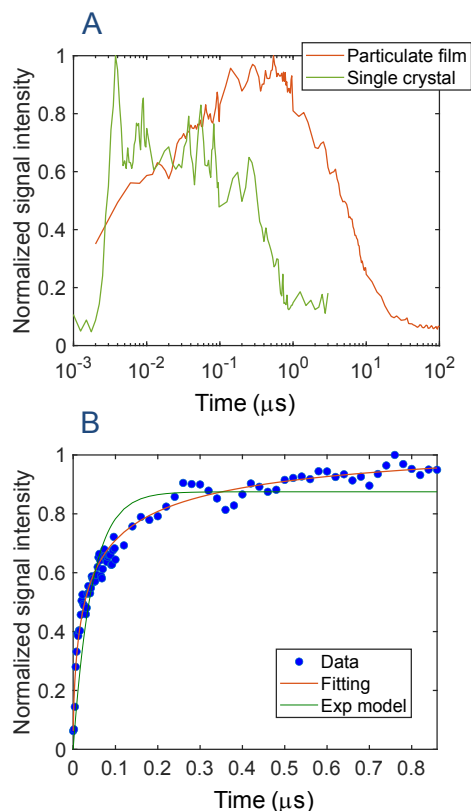


Figure 16 **A**: The normalized temporal responses of the refractive index change for the particulate film and the single crystal of TiO_2 are shown. The signal amplitude was calculated from the images of Fig. 15. **B**: The rising part of the TiO_2 particulate film and the fitting curve obtained from Eq. (4). The parameters were $S=18.2$ [-], $\beta=6.16$ [μm^{-1}], $D_N=0.594$ [$\mu\text{m}^2/\mu\text{s}$], respectively. For comparison, a fitting curve using an exponential model is also shown. Reproduced from ref. 102 with permission from MDPI, copyright 2021.

Building on this hypothesis, we applied our model to the signal data for the particulate film and successfully derived relevant parameters. These findings are displayed in Figure 16, where the response was accurately fitted ($R^2 = 0.97$). Notably, the response could not be aptly modeled using a simple exponential rise, as evidenced in the same figure. The signal response aligned well with our

proposed diffusion-trapping model. Similar outcomes were observed for SrTiO₃, Fe₂O₃, and BiVO₄. These results suggest that the diffusion-induced trapping of photo-excited charge carriers is a widespread occurrence in particulate photocatalytic materials, a phenomenon not detectable through conventional time-resolved techniques like TA and TP methods. The time-resolved method involving refractive index change serves as a complementary approach, capturing key processes in the dynamics of photo-excited charge carriers that other methods might miss.

3.3 Exciton dynamics observed for TiO₂ nanoparticulate film

86

Figure 17A presents a series of images capturing the changes in the refractive index of a nanoparticulate TiO₂ film over time. These images revealed a response that varied depending on location, with bright spots of approximately $2\text{-}3\pm 1$ μm in diameter emerging around 50 ± 10 ns. Through spectral clustering, the transient responses were categorized into three distinct groups, which are depicted in Figure 17B. The initial phase image of the sample, shown in Figure 17C, displays aggregations a few microns in diameter, yet these aggregates did not coincide with the rapid 50 ns responses.

For each category, the average responses from all pixels within the same group are presented in Figure 17D. The proportion of responses in each category was approximately 1:12:8. A comparison of Figure 17C and D reveals that the most extensive area (shown in green in the categorized map, #2 in B) corresponded to a response similar to the average response of photo-excited charge carriers with a decay time of about 10 μs . Interestingly, many areas showed no response (blue region, #3 in B), a detail that would have been missed without imaging the responses. An unusual response, characterized by a swift rise and fall within about 50 ns, appeared as spots in the red region (#1 in B). This suggests that the behavior of photo-excited charge carriers in these areas was markedly different from others.

This analysis demonstrates that while the majority of photo-excited charge carriers decayed around 10 μs , not all areas exhibited similar responses. In some regions, photo-excited charge carriers were not generated at all, while others showed rapid responses of about 50 ns. This pattern was consistent across all the areas examined.

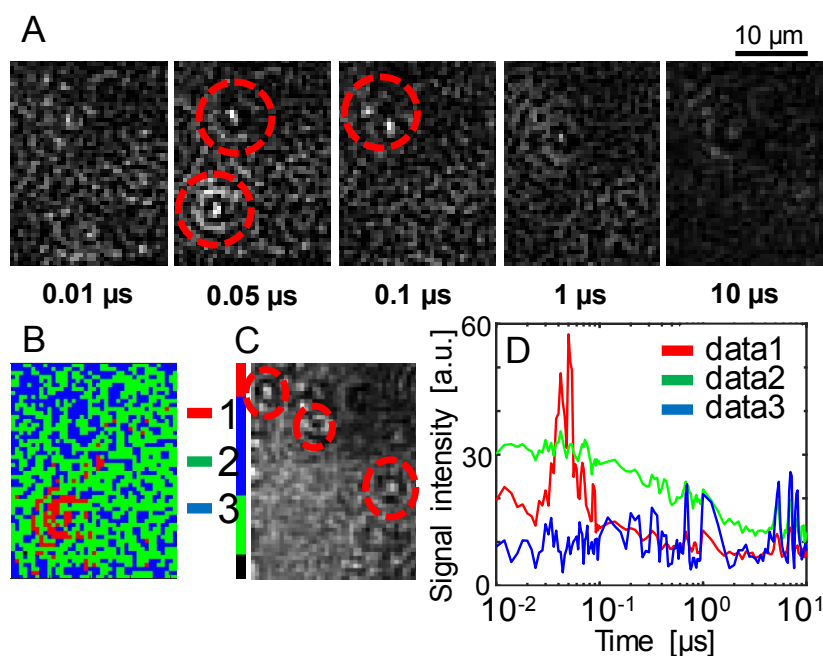


Figure 17 **A:** An image sequence of the refractive index response in a small region (25×20 nm) on the order from nanoseconds to microseconds. The scale bar corresponds to $10 \mu\text{m}$. The bright spot is indicated in red circles. **B:** The categorized mapping of the charge carrier responses of **A**. **C:** A microscopic image at the same area as **A**. The aggregation is indicated in red circles. **D:** The averaged responses for each categorized response. Reproduced from ref. 86 with permission from American Chemical Society, copyright 2020.

Regarding the average response, the microsecond dynamics observed in TiO_2 particulate films are generally attributed to the recombination of electrons and holes trapped on the surface.^{7,11,33} However, the nanosecond dynamics of photo-excited charge carriers in these films remain less understood, differing from the dynamics in single crystalline TiO_2 .²⁶ In semiconductor oxides, photo-excited charge carriers are often trapped in surface or interface states within a femtosecond to picosecond timeframe,^{7,35} and their dynamics on the nanosecond scale vary based on the sample's condition. While reactions of photoexcited holes at interfaces have been indicated,^{7,36} such interfacial charge transfer was prevented by the contact between TiO_2 and ACN in this study.

A likely explanation for the observed nanosecond response is a faster recombination pathway via self-trap exciton states (STEs).³⁷ Excitonic polarons, observed through photoluminescence measurements, occur when electron and hole polarons are trapped by surface states, forming weakly-bound STEs.³⁸ In TiO_2 , if the Coulomb interaction between electrons and holes is sufficiently strong, they stay close enough for radiative recombination. The STEs have a lifetime ranging from 0.5 to 3

μs .^{39–42} (The spotty responses were not due to the emission). Also, the radiative decay of STEs is much weaker at room temperature,^{40–42} where mobile electrons can escape the exciton state, reducing radiative recombination. We suggest that these observations represent 'nonradiative' recombination processes of STEs, corroborated by the nonlinear increase in spot numbers with increased pump intensity. It's reported that electron polarons can migrate to where the immobile hole polaron is located, forming self-trapped excitons within nanoseconds. The spotty local response could be explained by the random encounter of electron and hole polarons.⁴⁰

This research marks the inaugural observation of nonradiative decay in self-trapped excitons within semiconductor materials at room temperature. Prior to this, similar phenomena had only been reported in specific contexts, such as with alkali halides⁴³ and lanthanum halides⁴⁴. Our findings reveal that relying solely on the 'average' temporal response is inadequate for a comprehensive understanding of photo-excited charge carrier behavior in semiconductor particulate films. This inadequacy is primarily due to the presence of defects that are both locally and sparsely distributed across various dimensional scales. Uncovering the relationship between the local structure of these materials and the behavior of charge carriers holds significant potential. It could lead to valuable insights that enhance the efficiency of photocatalytic materials, ultimately guiding their structural refinement and optimization.

3.4 Scavenger study for charge carrier distinction for titanium oxide and hematite¹⁰⁹

The PI-PM image sequence and its analysis by the clustering helps understand the charge carrier types by comparison of the charge carrier mapping with/without scavengers. By the clustering analyses of all the pixel-by-pixel responses, we could extract various different charge carrier dynamics because photocatalytic materials have inhomogeneity on film surfaces and the charge carrier behavior depends on the local structure and species. Even for typical photocatalytic materials, TiO_2 and hematite, we could recognize various charge carrier dynamics, which cannot be differentiated by the general fitting procedure for the averaged time response. We could categorize the surface-trapped charge carriers (holes and electrons) and bulk carriers in the nanosecond to millisecond order, which indicates that this analytical procedure will play an important role in understanding the charge carrier dynamics for various photocatalytic materials.

The image sequence data (three-dimensional data (space and time)) is recovered by the 3DTV.¹¹⁰ In the analysis of the data, the temporal responses at all the pixels (> 10000) in a PI-PM image sequence are categorized in terms of the local charge carrier responses by the clustering analysis. The response shapes are compared and the similarity is used for the categorization of the types of charge

carriers. The category map of the types of charge carriers could reveal the position-dependence.

A liquid layer on a film was prepared by putting another glass slide together with a silicon rubber spacer (thickness: 0.5 mm). Acetonitrile (ACN), ethanol (EtOH), and 0.1 mM nitrobenzene (NB)/EtOH was inserted into the gap. ACN was used as an inert liquid, indicating no charge transfer from photocatalytic materials to the liquid side,⁶¹ otherwise, photo-excited electrons are scavenged by oxygen in air or solutions. EtOH was used as a hole scavenger, and NB/EtOH was used as an electron-and-hole scavenger. We revealed that NB was converted into nitrosobenzene in the photocatalytic reaction,¹⁰⁰ under the hole scavenging condition (in ethanol). This means that nitrobenzene works as an electron scavenger and ethanol works as a hole scavenger. We could not find an optimal scavenger that works only for electrons under the pulse-light illumination condition. A typical electron scavenger, Ag^+ , was photo-reduced to form nanoparticles on the substrates, which affected the signal response, and Fe^{3+} cannot be used because it is a colored solution for the pump light.

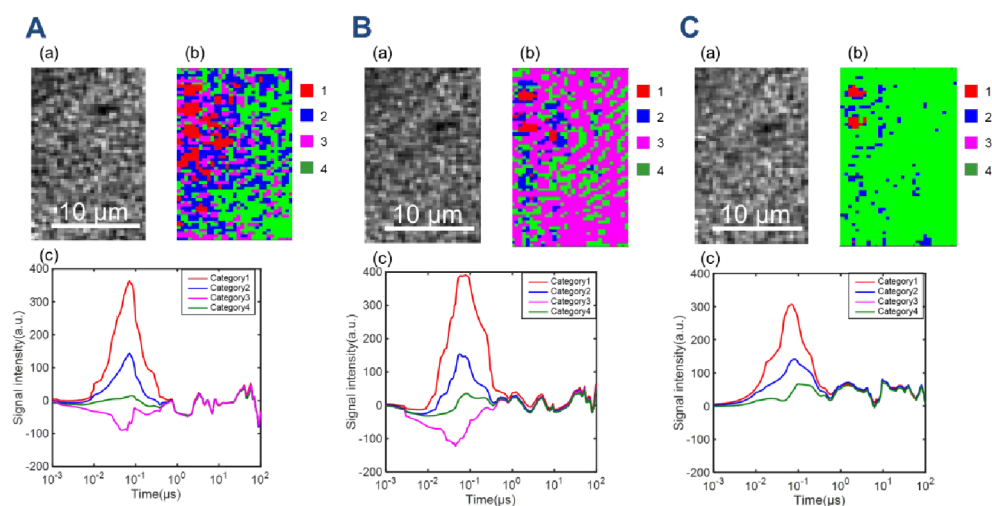
Here we show an example for a region ($25 \times 60 \mu\text{m}$) of a hematite photoanode, Fe_2O_3 , was used for analysis. Time-resolved image sequences for a Fe_2O_3 film in contact with three types of solvents (ACN and EtOH, and NB/EtOH) were measured in the same region by the PI-PM method. The PI-PM image sequence was measured for 0 ns – 100 μs under photo-excitation with a stripe pattern in a larger area. The photo-irradiated regions showed an inhomogeneous contrast from 1 ns followed by an unclear increase/decrease, and decayed until a few hundreds of nanoseconds. It seems that a positive (whitish) contrast was apparent in ACN until around 10 ns, compared with those in EtOH. But the final decay time was < 500 ns for all the solvents. To make an assignment of charge carrier dynamics, the clustering of the charge carrier dynamics was studied in a smaller region.

Time-resolved image sequences for a Fe_2O_3 film in contact with three types of solvents (ACN and EtOH, and NB/EtOH) were measured in the same region by the PI-PM method. In the PI-PM image sequence, the photo-irradiated regions showed an inhomogeneous contrast from 1 ns followed by an unclear increase/decrease, and decayed until a few hundreds of nanoseconds. It seems that a positive (whitish) contrast was apparent in ACN until around 10 ns, compared with those in EtOH. But the final decay time was < 500 ns for all the solvents.

The clustering of the charge carrier dynamics was studied. Figure 18 shows the categorized maps of the charge carrier responses of $\alpha\text{-Fe}_2\text{O}_3$ film. We recognized four types of responses in $\alpha\text{-Fe}_2\text{O}_3$ film in ACN; A positive-strong response (Category 1), a positive response (Category 2), a negative response (Category 3), and no response (Category 4) were categorized. The ratio of the four categories in this region was 10, 33, 19, and 38 %, respectively. When the solvent was changed to EtOH, the categories were the same as those in ACN, but the ratio drastically changed; 2, 9, 62, and 27 % for the four categories. The positive responses (Categories 1 and 2) were reduced and changed into negative responses (Category 3). (The difference between Category 1 and 2 is only the intensity difference, corresponding to the density difference of the photoexcited carriers.) This result clearly indicates that

the positive response was due to photo-excited holes, which were scavenged by EtOH. By replacing the solvent with NB/EtOH, the negative response (Category 3) could not be detected, and only Categories 1,2 and 4 were recognized. However, it is noted that most of the signals were lost and changed into no response (Category 4), judging from the ratio of the categories; 2, 6, 0, and 92 %, respectively. From the effect of the electron scavenger, the negative response (Category 3) was due to the electron response. It is noted that the electron response showed a faster response than holes (the negative response showed an initial decrease around a few nanoseconds, while the positive response started to increase after 10 ns.)

Figure 18 The categorized maps of the charge carrier responses of an α -Fe₂O₃ film in **A**: ACN,



B: EtOH, and **C**: NB/EtOH. (a) corresponds to a microscopic image, and the corresponding categorized map is shown in (b). The averaged responses for three categories are shown in (c). Reproduced from ref. 109 with permission from MDPI, copyright 2022.

It seems that the photo-excited electrons appeared faster around a few nanoseconds, almost the same as the pulse width, and the holes were observed after 10 ns. Both of the responses decayed within a few hundred nanoseconds. It is supposed that the rising and falling parts for the positive and negative responses correspond to the hole and electron trapping to the surface states, based on the slow rising/falling responses on the order of nanoseconds. This was studied well in the previous study that it takes time for the photo-excited charge carriers to reach the surface states during the diffusion for photocatalytic particulate films.¹⁰² In short, the photo-excited electrons and holes were trapped to the surface states with time constants of 10-30 ns, and the trapping process was faster for electrons, and they recombined about 200-300 ns.

Here, we showed demonstration applications of the PI-PM method combined with the clustering analysis for hematite, and the similar analysis for TiO₂ was also valid. It is usually difficult to assign

different types of charge carriers only from the time-resolved response, even from the effect of various scavengers for each charge carrier. However, in the PI-PM method, the charge carriers were categorized by the charge carrier responses, which were returned back to the surface map of different charge carrier types. By investigating the charge carrier maps for different scavengers, the charge carrier types are usually more obvious compared with the general procedure such as a response change due to the scavengers. In a sense, the charge carrier response was originally averaged, which could include various different responses, especially for the inhomogeneous samples such as photocatalysts and photovoltaics, but using a huge number of the charge carrier responses and the clustering analysis, the data dimension was expanded, and more useful extension of the data is available. These demonstration experiments could convince you to use the data effectively to understand the charge carrier dynamics for photocatalytic and photovoltaic materials.

3.5 Photocatalytic activity study on photoanode and photocathode materials¹⁰⁹

Photocatalytic water splitting is an emerging method for producing clean hydrogen and has been explored using various materials. Understanding charge carrier dynamics is a key to comprehending the mechanisms of interfacial reactions. However, the inhomogeneous reactions caused by particulate materials have complicated the differentiation of charge carrier types. The PI-PM method has been employed to analyze local charge carrier dynamics. We focused on two materials used in particulate photocatalyst sheets for Z-Scheme overall water splitting: Rh-doped SrTiO₃ (STOR) and Mo-doped BiVO₄ (BVOM), which serve as hydrogen and oxygen evolution materials, respectively. By mapping the distribution of charge carrier types and analyzing their behavior in the presence of scavengers, we were able to spatially isolate and identify local charge carriers relevant to water-splitting, providing insights into surface-trapped charge carriers.

The PI-PM method proved effective in identifying charge carrier processes by differentiating between types of charge carriers and assessing the variation in carrier types with and without a scavenger. We studied STOR and BVOM photocatalyst films to demonstrate this charge carrier assignment. Our detailed analyses yielded comprehensive information on the charge carrier dynamics for each material, clearly distinguishing between different types of charge carriers. ACN and EtOH served as an inert liquid and a hole scavenger, respectively. The average responses in both solvents showed no significant difference. We selected regions of 30 x 40 μm for STOR and 40 x 40 μm for BVOM within the illuminated areas. The category map was then reconstructed based on the local positions to depict the distribution of charge carrier types.

A specific example for STOR in contact with ACN is presented in Figure 19A(a-d). The initial PI-PM image sequence is shown in (a). Analysis of the image sequence data (image: 65 x 105 pixel) (Figure 19A(b)) revealed three types of responses. The locations corresponding to each response were mapped out in Figure 19A(c), alongside an optical image obtained using the same setup in the same area (Figure 19A(d)). Category 1 exhibited a rapid response with rise-and-decay times of 30-40 ns and ~200 ns, respectively. Category 2 displayed rise-and-decay times of 700-800 ns and ~10 μ s. Additionally, Category 3 showed no response. Category 1 was associated with intrinsic recombination, while Category 2 was linked to hole accumulation at Rh sites (Rh^{3+} to Rh^{4+}), as identified in previous studies, because time-resolved study revealed that this component was scavenged by a hole scavenger and also the Rh species has an ability of hole accumulation.^{87,104} Similar slow hole decay has been reported in other studies involving metal doping for STO.^{26,47} The area ratios for Categories 1, 2, and 3 were 15%, 51%, and 32%, respectively. The sites of hole accumulation due to Rh doping were widespread, whereas areas of intrinsic recombination were more localized.

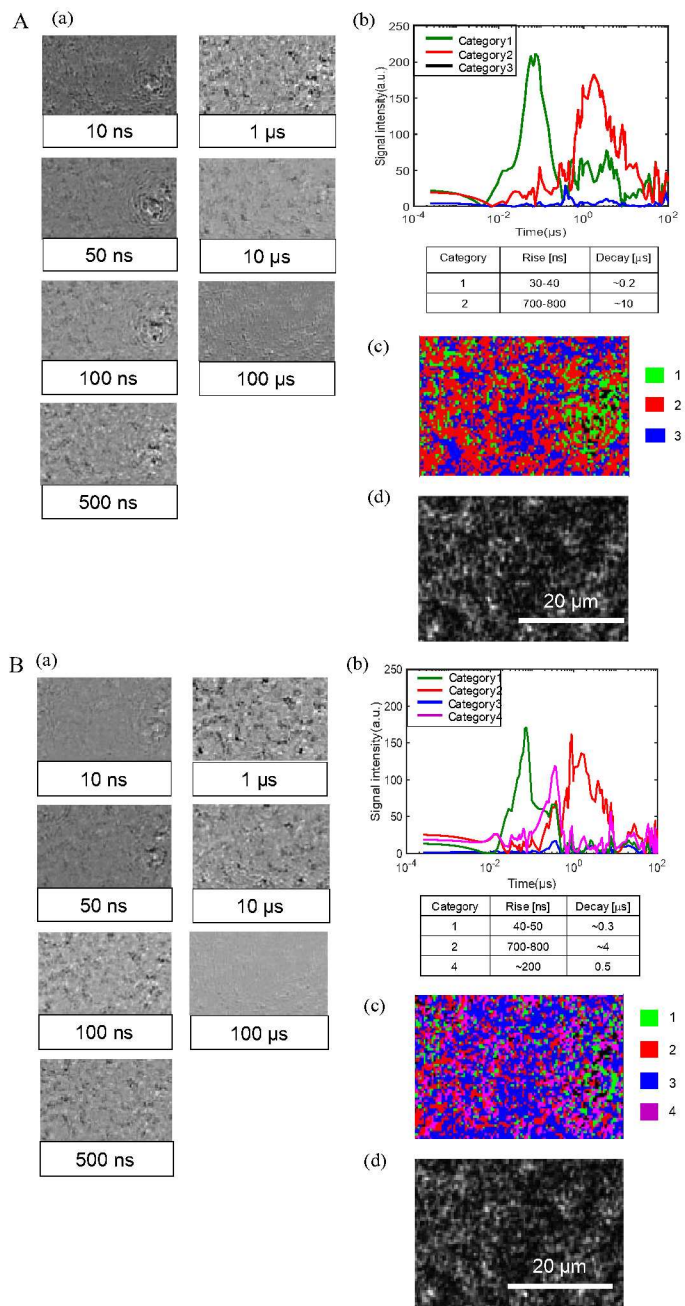


Figure 19 A: The image sequence for STOR in ACN by the PI-PM method and the results by the clustering analyses are shown in (b) and (c); (b) the average response for each category and the time constants for the rise-and-decay of the categorized responses, and (c) the corresponding categorized map (green: Category 1, red: Category 2, blue: Category 3, purple: Category 4) (d) A microscopic image in the same region is shown. The scale bar corresponds to 20 μ m. The sample was STOR in

contact with ACN. **B**: The same result in MeOH is shown. Reproduced from ref. 111 with permission from American Chemical Society, copyright 2022.

This analysis was similarly conducted for STOR in MeOH, with the results displayed in Figure 19B(a-d). Like with ACN, three categories were identified (Figure 19B(b)); Category 1 with rapid response times of 40-50 ns and ~300 ns, Category 2 with 700-800 ns and ~4 μ s, and no response in Category 3. Since the time constants for Categories 1 and 2 closely matched those in ACN, the same interpretations were applied. Notably, a new Category 4 was distinguished, characterized by rise-and-decay times of ~200 ns and ~500 ns. The distribution of responses was 11% for Category 1, 22% for Category 2, 47% for Category 3, and 17% for Category 4. The locations corresponding to Category 4 mainly originated from the areas of Category 2 in Figure 19A(c). Therefore, it was concluded that Category 4 in MeOH evolved from Category 2.

Considering that Category 2 represents the hole trapping state at the Rh sites, which can be scavenged by methanol, it likely transformed into Category 4 due to methanol removing the oxidized Rh⁴⁺ state. The intrinsic recombination (Category 1) remained unaffected by the hole scavenger. For water splitting, surface-trapped electrons recombine either with the remaining oxidized Rh state (Category 2) or with surface-trapped holes if the oxidized Rh state is scavenged by methanol (Category 4).

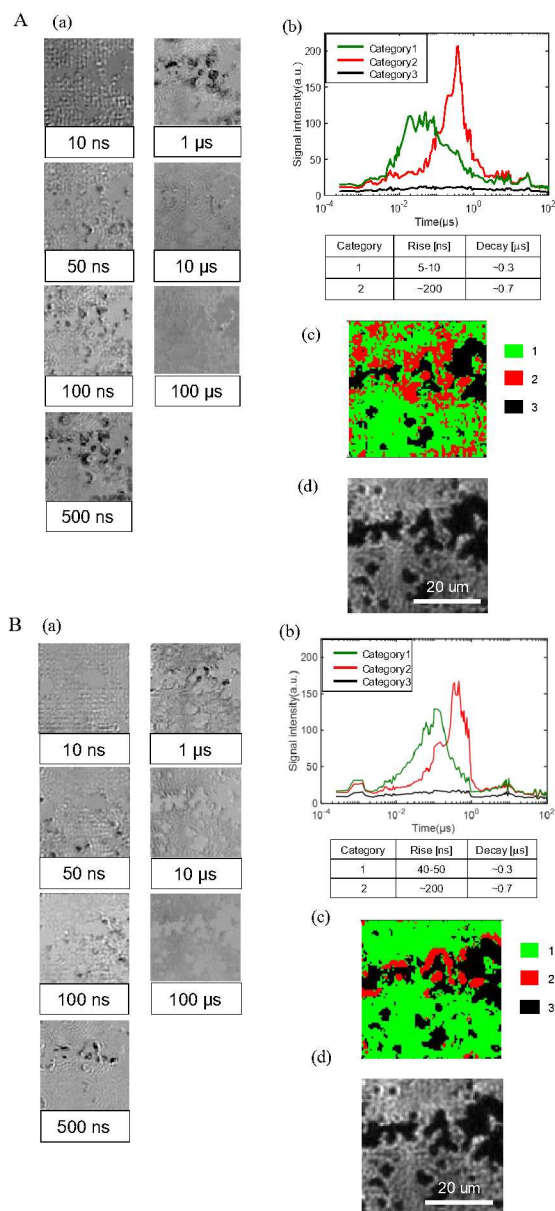
Similarly, local charge carrier dynamics were analyzed for BVOM, as shown in Figure 20A(a-

d). The original PI-PM image sequence (image 80 x 80 pixel) is depicted in Figure 20A(a), revealing

three types of responses (Figure 20A(b)). The categories for each response type were mapped in Figure

20 A(c), alongside an optical image (Figure 20A(d)). Category 1 displayed rapid response times of 5-

10 ns and ~ 300 ns, while Category 2 had ~ 200 ns and ~ 700 ns for rise-and-decay. Additionally,



Category 3 showed no response. Categories 1 and 2 were associated with intrinsic recombination and recombination of surface-trapped holes, respectively, from previous studies.⁸⁷ The latter is linked to the water-splitting reaction and aligns with reports on the lifetimes of surface-trapped holes in BiVO_4 , ranging from nanoseconds to microseconds.^{28,50,112,113} Category 3 indicated areas with no excited charge carriers. The area ratios for Categories 1, 2, and 3 were 58%, 23%, and 19%, respectively. The locations of Category 3 corresponded to material aggregates, which allowed minimal light transmission. The areas of intrinsic recombination were widely distributed, while the surface-trapped holes were more localized.

Figure 20 **A**: The image sequence for BVOM in acetonitrile by the PI-PM method and the results by the clustering analyses are shown in (b) and (c); (b) the average response for each category and the time constants for the rise-and-decay of the categorized responses, and (c) the corresponding categorized map (green: Category 1, red: Category 2, black: Category 3) (d) A microscopic image in the same region is shown. The scale bar corresponds to 20 μm . **B**: The same result in MeOH is shown. Reproduced from ref. 111 with permission from American Chemical Society, copyright 2022.

The same analysis was applied to BVOM in MeOH, as shown in Figure 20B(a-d). Here, two distinct response types were identified (Figure 20B(b)): one being a rapid response with rise-and-decay times of 40-50 ns and ~ 300 ns, and the other a slower response with ~ 200 ns and ~ 700 ns. Comparing these with the responses in Figure 20A(b), the reaction in Category 1 slowed down, while the reaction in Category 2 remained relatively unchanged. The distribution of these categories was 68% for Category 1, 8% for Category 2, and 24% for Category 3. Notably, there was an increase in Category 1's ratio and a decrease in Category 2's, compared to the category map in Figure 20B(c). Moreover, the locations for Category 2 in Figure 20B(c) were predominantly near the BVOM aggregates, as seen in Figure 20B(d).

This suggests that the areas experiencing recombination of surface-trapped holes were diminished because methanol scavenged these holes, transforming the distributed surface trap sites into regions of intrinsic recombination. Two recombination processes were observed: intrinsic recombination and recombination of surface-trapped holes, with the latter being scavenged by methanol. The delay in intrinsic recombination, caused by methanol's reduction of holes, led to fewer recombination opportunities for electrons. Although methanol scavenged the surface-trapped holes, the sites near the aggregates were not affected.

This study demonstrates categorization of charge carrier types using clustering analysis on time-resolved microscopic image sequences for two photocatalytic materials: Rh-doped SrTiO_3 and Mo-doped BiVO_4 , both used in 'Z-Scheme' overall water splitting. Typically, the characterization of charge carriers involves observing changes in time-resolved responses upon adding scavengers. However, identifying charge carriers based solely on 'average' time-resolved responses can be ambiguous. Our PI-PM method enabled observation of charge carrier responses at each microscopic location, categorizing them based on response similarities. By analyzing how the charge carrier type map changes with scavengers, we could more accurately assign charge carrier types. This approach is crucial for understanding local charge carrier dynamics and their relation to the local structure.

3.6 Photocatalytic activity analysis for BVOM/ITO/STOR Z-

scheme photocatalytic sheet ⁸⁷

Sunlight-driven water splitting into hydrogen and oxygen represents a highly promising avenue for clean energy generation. ^{17,114,115} Significant efforts have been directed towards the development of suitable materials for this purpose. These endeavors have also expanded into the realms of device fabrication and large-scale implementation. ^{116,117} In the context of overall water splitting, it's crucial to select materials with appropriate band positions for both the reduction of protons and the oxidation of water. To facilitate these reactions, co-catalysts are often employed. Rather than relying on a single material, a common approach involves using two different materials in tandem for generating hydrogen and oxygen. This method, where charge transfer between the two materials compensates for remaining charges, is known as the 'Z-scheme water splitting system.' ^{17,114,118–120}

In employing the Z-scheme strategy, a variety of semiconductor combinations are explored. A popular pairing is Mo-doped BiVO₄ (BVOM) and Rh-doped SrTiO₃ (STOR), serving as catalysts for oxygen and hydrogen generation, respectively. Recently, a type of photocatalyst sheet—designed for easy production through extensive screen-printing methods and incorporating a conductive colloidal binder (like Au, ITO)—has been developed. This sheet features a densely packed film structure, enhancing its suitability for broader deployment. ^{21,121,122}

This photocatalyst sheet was analyzed using the PI-PM method in ACN and EtOH. Through detailed investigations into the effects of scavengers (water, ethanol for each component), the time responses were classified into three distinct processes based on their timescales. Figure 21 illustrates how photo-excited charge carriers are generated in the conduction and valence bands following excitation, as the wavelength of the pump laser (355 nm) exceeds the bandgap energy of both materials (BiVO₄=2.4 eV, SrTiO₃=3.2 eV). We monitored the dynamics of these charge carriers after interband transition in both materials. The carriers are quickly trapped in shallow or deep states due to various types of defects, typically completing within the picosecond timeframe. ^{50,103,105,113} These trapped carriers then decay, either recombining within the materials or being extracted externally. The first component of the response encompasses these rapid charge carrier dynamics. As ACN acts as an inert solvent for charge carriers, they remain confined within the materials for longer periods. This results in a response observed over hundreds of microseconds, corresponding to the microsecond recombination process for BiVO₄ and SrTiO₃, ^{26,48} which is included in the third component of the response.

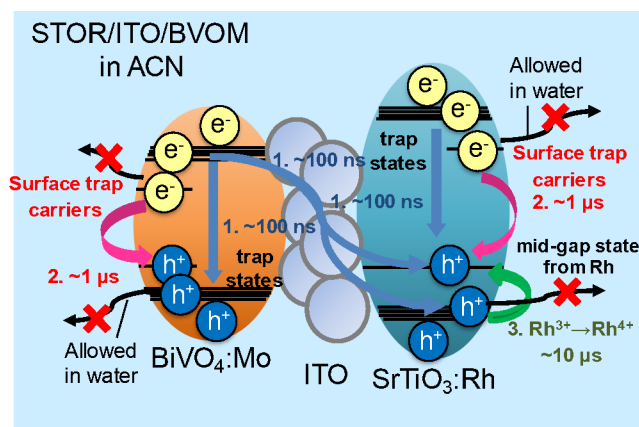


Figure 21 This scheme corresponds to the charge transfer diagram in SrTiO₃:Rh/ITO/BiVO₄:Mo (STOR/ITO/BVOM) in acetonitrile (ACN). Step 1 includes intrinsic recombination inside materials and charge transfer between two materials. Step 2 indicates the decay of surface-trapped charge carriers in ACN, which are utilized for water-splitting reactions with water outside. Step 3 includes the hole trapping to Rh^{3+/4+} state in STOR and the slower recombination. Surface-trapped carriers cannot be transferred to the solution side in ACN, where all processes of charge dynamics are completed in the system. Reproduced from ref. 87 with permission from Springer Nature, copyright 2021.

The second component in our analysis was associated with electrons in STOR or holes in BVOM located on the film surfaces, as these surface-trapped charge carriers were engaged in water-splitting reactions through their consumption by water. The absence of this component in the presence of water suggests that the corresponding charge carriers were actively involved in water-splitting reactions. This is supported by the high water-splitting efficiency of this photocatalytic sheet even with pure water. Conversely, this result also indicated that surface-trapped carriers were effectively utilized in water in this system.

We observed that these second components (ranging from 100 ns to 1 μs) were present in ACN for both materials but disappeared in water, reinforcing the idea that these components represented holes in BVOM and electrons in STOR used in water-splitting reactions. It seemed that the holes in BVOM and electrons in STOR for water splitting coincidentally matched in their lifetimes, resulting in a combined response in the Z-scheme sample. Additionally, we noted a delay in the second rising component up to 10 μs in STOR in ACN. This delay might be due to the mid-gap state in STOR related to the Rh^{3+/4+} state within the bandgap,^{104,123} which is crucial for visible light absorption. The delayed response in STOR when in ACN suggested unique components of photo-excited charge carriers due to the absence of water-splitting reactions in ACN.

Figure 22 presents the PI-PM results for the Z-scheme sample. The transient responses were grouped into three categories through spectral clustering¹²⁴ and mapped in Figure 22A(b). Outliers, significantly different from these three categories, were marked as #0 (black) in this map. The original microscopic phase image of the sample, captured without pump pulse irradiation using the same optical setup as the PI-PM method, is shown in Figure 22A(c) and features micron-sized aggregates.

For each category, the average responses from all pixels within the same category are displayed in Figure 22A(d). The categorized map in Figure 22A(b) and (d) predominantly consisted of red and blue regions. The red region's response was akin to an averaged overall response (data 1 in (d)), while the blue response appeared to be a mix of the first and third responses (data 2 in (d)). A minor portion of green regions in Figure 22A(b) corresponded to a slow rising component (data 3 in (d)), indicative of the third component. From our earlier assignment, the response of data 1 in Figure 22A(d) comprised intrinsic recombination and the decay of surface-trapped carriers until 1 μ s, which are vital for water-splitting reactions. Hence, water-splitting reactions predominantly occurred in the red region. The blue response involved intrinsic recombination with hole decay to the Rh^{3+} state (Rh^{4+} formation) in STOR. The green regions, representing Rh^{4+} formation in Figure 22A(d), were significantly smaller compared to the red and blue regions, suggesting that the blue and green regions lacked water-splitting activity.

An identical analysis was performed on a Z-scheme sample without the ITO mediator (STOR/BVOM) to evaluate the effect of ITO, as shown in Figure 22 B. Similar categories of transient responses were observed. However, the green regions in the categorized map (Figure 22B(b)) increased drastically, while the red regions reduced significantly compared to Figure 22B(b). The proportion of the blue region remained mostly unchanged. These findings implied that the area of Rh^{4+} formation increased substantially in the absence of an ITO mediator, which explained why the water-splitting reaction was less efficient in this system.

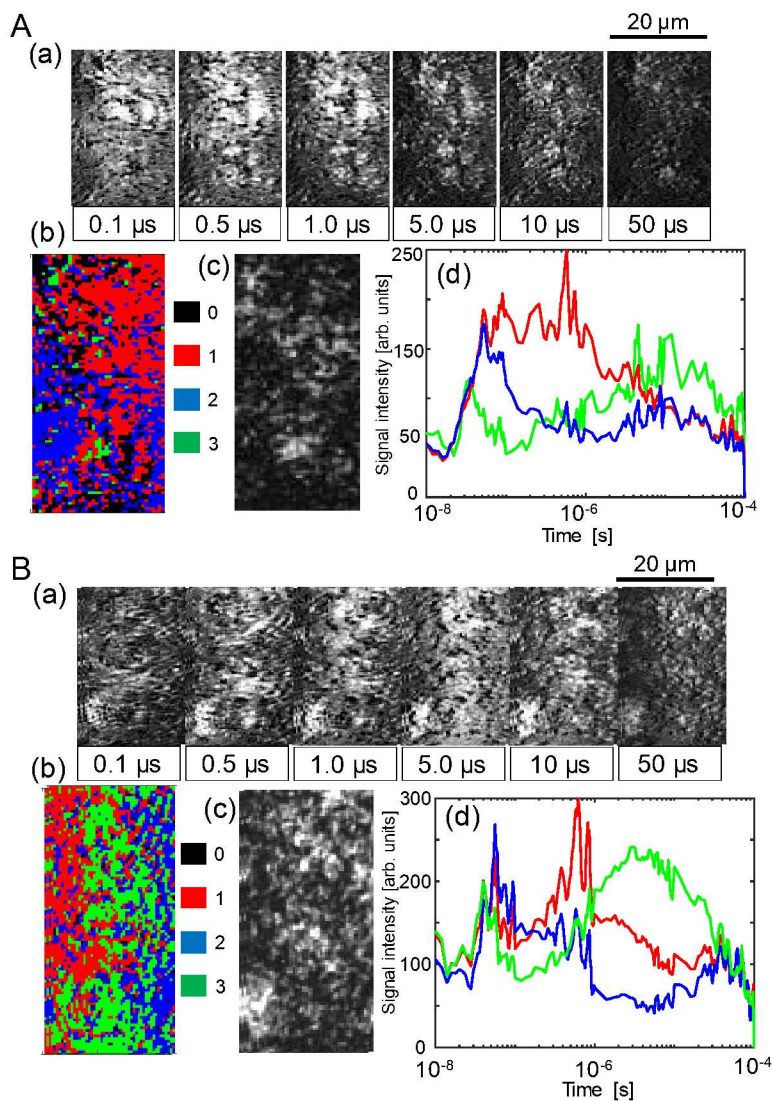


Figure 22 A: (a) An image sequence of the refractive index change for SrTiO₃:Rh/ITO/BiVO₄:Mo (STOR/ITO/BVOM) in acetonitrile (ACN) in a square region ($20 \times 50 \mu\text{m}$) on the order from nanoseconds to microseconds. The scale bar corresponds to $20 \mu\text{m}$. (b) The categorized mapping of the charge carrier responses of a. An outlier positioned far from all categories was colored in black (#0). (c) A microscopic image in the same area as in a. d The averaged responses for each category in b are shown. (red: category 1, blue: category 2, green: category 3). B: The same analysis was performed for SrTiO₃:Rh/BiVO₄:Mo, which does not include an ITO layer. Reproduced from ref. 87 with permission from Springer Nature, copyright 2021.

The combination of the PI-PM and the clustering analysis could visualize reactive sites for efficient water-splitting reactions and inactive sites deteriorating water splitting efficiency. This technique will be a powerful tool for the detection of active/inactive sites for the water-splitting

materials but also the other materials involving electron transfer reactions providing swift optimization for photocatalytic materials.

3.7 Cocatalyst activity analysis for photocatalytic materials ¹²⁵

The $\text{La}_5\text{Ti}_2\text{Cu}_x\text{Ag}_{1-x}\text{S}_5\text{O}_7$ series (where x ranges from 0 to 1) are oxysulfides known for their strong absorption in the 550 to 750 nm range. These materials are p-type semiconductors, primarily due to copper species acting as acceptors, ¹²⁶ and have drawn significant attention for their potential in photoelectrochemical and photocatalytic hydrogen production. ^{127–130} Enhancements in their photocatalytic efficiency were achieved by substituting titanium with gallium, thus increasing electronic conductivity. ¹³¹ The impressive performance of gallium-doped $\text{La}_5\text{Ti}_{2-x}\text{CuS}_5\text{O}_7$ in photoelectrochemical applications led to its use in tandem/parallel photoelectrochemical cells and photocatalyst sheets for independent water splitting. ^{131,132} Cocatalysts, often used to improve charge separation and catalyze surface reactions in photocatalytic water splitting, have been variously applied to these materials, although their effects on particulate photocatalytic substances remain somewhat ambiguous. ^{133–135} In this study, we employed the PI-PM method to examine local charge carrier dynamics in particulate gallium-doped $\text{La}_5\text{Ti}_{2-x}\text{CuS}_5\text{O}_7$, identifying different types of charge carriers through the scavenger effect and analyzing the impact of cocatalysts accordingly.

We conducted clustering analysis on the photo-excited areas to determine the nature of charge carriers. Previous research revealed that scavenger effects are localized on a micro-scale, helping the identification of charge carrier types by contrasting responses with and without scavenger effects. ¹¹¹ To differentiate between carrier types, we compared response shapes and intensities across specific regions, categorizing them into distinct groups based on these comparisons.

Figure 23 presents the categorized response maps for gallium-doped $\text{La}_5\text{Ti}_{2-x}\text{CuS}_5\text{O}_7$ in both ACN and MeOH. Three types of responses were observed: positive, no response, and negative, correlating well with certain regions in the optical images of the particles, suggesting that these responses originated from the particles or their aggregates. Interestingly, the positive and negative responses in these images indicated different origins of charge carriers, as inferred from their contrasting refractive index changes.

The distribution of these response categories differed between ACN and MeOH. In ACN, the ratios were 15%, 65%, and 21% for Categories 1, 2, and 3, respectively, while in MeOH, they shifted to 4%, 76%, and 20%. This shift, particularly the decrease in Category 1 and increase in Category 2 in MeOH, was attributed to the effect of the hole scavenger (MeOH), with Category 1 being identified as hole responses. It is hypothesized that the hole-excited regions were deactivated in MeOH, transforming into Category 2. Consequently, Category 3 was associated with electrons, the counterparts to holes.

The study also noted that Categories 1 and 3 responses are indicative of surface trapping and

subsequent recombination of holes and electrons. The recombination process for electrons was delayed in MeOH, likely due to a reduction in the number of holes. Interestingly, while the depletion of holes was faster in MeOH, the response of the remaining holes, presumably trapped at surface states, was slower. This slowdown could be a result of limited available surface states, which become occupied by trapped holes. This differentiation in charge carrier types revealed that the locations of surface-trapped electrons and holes varied, indicating spatial separation of charge carriers within the particles.

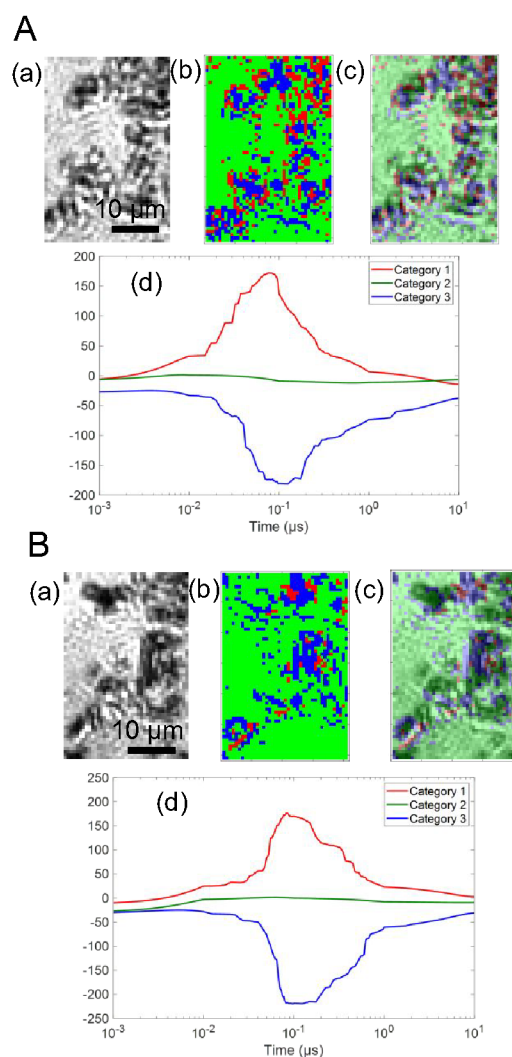


Figure 23 The categorized mapping of the charge carrier responses of LTCA in **A**: ACN and **B**: MeOH. (a) corresponds to a microscopic image and the corresponding categorized map is shown in (b). (c) is an image of the overlap between (a) and (b). The averaged responses for three categories are shown in (d). Reproduced from ref. 125 with permission from Royal Society of Chemistry, copyright 2022.

Figure 24 illustrates the response maps of charge carriers for rhodium-doped oxysulfide (Rh/Ga-LTCA) in ACN. In this setting, four distinct types of responses were identified, one more compared to Ga-LTCA alone. These responses included a positive response (Category 1), no response (Category 2), and two different negative responses (Categories 3 and 4). Comparing these findings with Ga-LTCA and considering the effect of MeOH as a scavenger, it was deduced that Categories 1 to 3 correspond to the same phenomena observed in Ga-LTCA: surface-trapped holes for Category 1 and surface-trapped electrons for Category 3. Category 4 emerged as a novel component, representing a delayed response compared to Category 3. Rhodium, acting as a cocatalyst, gathers electrons and is known to facilitate electron transfer to cocatalyst sites in microseconds.¹³⁶ Therefore, it was hypothesized that the responses in Category 4 were related to electrons trapped at Rhodium sites.

The negative responses were divided into two types: one similar to Ga-LTCA and the other showing a slower reaction. The time constants for the fall-and-recovery component were 20-30 ns and 700-800 ns for Category 3, and 60-70 ns and 1-2 μ s for Category 4. The addition of a cocatalyst for electrons resulted in some electrons being trapped at Rh sites, leading to a delayed electron response. These observations suggest that the trapping and recombination processes of charge carriers, with opposite signs and at different sites, can influence each other. This implies that Rh not only enhances charge separation but also alters the nature of charge carriers, particularly extending the lifetime of electrons, which is beneficial for reduction reactions.

In terms of area coverage, Categories 3 and 4 constituted 24% of the total area, with a ratio of 2:8 between them. Similar proportions were observed in other regions, indicating that Rhodium effectively influenced about 70-80% of the electron-excited areas. Despite the optimization of Rh deposition for maximum efficiency, it is possible that some Rh sites did not fully cover all electron-accumulating areas or some Rh did not function as an effective electron mediator in its cocatalyst role.

Our research revealed that on a micron scale, surface-trapped electrons and holes within particles and aggregates were distinctly separated. The influence of Rh as a cocatalyst was evident, marked by a change in electron dynamics compared to Ga-LTCA alone. Notably, 70-80% of the electrons followed an alternative route involving trapping at Rh sites, which resulted in a prolonged lifetime. Despite the Rh deposition being optimized, there remains a potential for enhancing the cocatalyst effect by 20-30%. Through this approach, we gained a comprehensive understanding of how cocatalysts influence carrier behavior in various photocatalytic particles and films. This knowledge can guide the optimization of a blend of different materials, such as the overall photocatalytic substances, the quantity of cocatalysts, and defect passivation strategies.

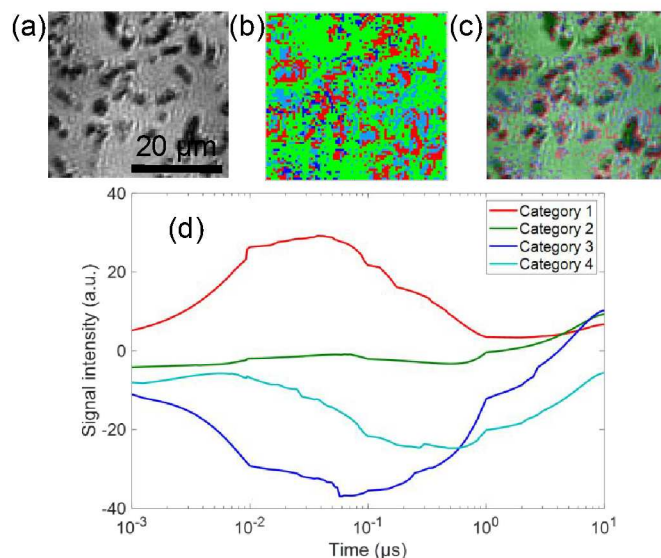


Figure 24 The categorized mapping of the charge carrier responses of Rh/LTCA in ACN. (a) corresponds to a microscopic image and the corresponding categorized map is shown in (b). (c) is an image of the overlap between (a) and (b). The averaged responses for three categories are shown in (d). There were four types of response in Rh/LTCA in ACN; positive response (category 1), no response (category 2), faster negative response (category 3), and slower negative response (category 4). The ratio of Rh active and Rh nonactive region was 80.0% and 20.0%. Reproduced from ref. 125 with permission from Royal Society of Chemistry, copyright 2022.

3.8 Application for photovoltaic perovskite materials^{82,137}

Building on the initial breakthroughs in organometal halide perovskites for solar energy applications,^{3,138} this material class has seen extensive global research. The latest devices are nearing a power conversion efficiency (PCE) of 25%.¹³⁹ Beyond photovoltaic uses, these perovskites are also key in highly sensitive photo-detectors^{140,141} and light-emitting quantum dots,^{142,143} with expanding applications.

Various time-resolved techniques have been employed to study the charge carrier dynamics in perovskite solar cells (PSCs).^{144,145} These studies, including time-resolved photoluminescence (PL) and transient absorption (TA), reveal the dynamics of charge carrier recombination, influenced by mechanisms such as Shockley-Read-Hall (SRH) and bimolecular recombinations.^{146,147} PSCs exhibit notably long charge carrier lifetimes, ranging from hundreds of nanoseconds to microseconds,¹³⁹ due in part to certain defect states that do not significantly impact charge recombination.¹⁴⁸ This results in an unusually long diffusion length for the charge carriers. During decay processes like recombination, charge carriers diffuse depending on grain size, with over-grain diffusion on the order of 100 picoseconds.¹⁴⁹

A common preparation method, anti-solvent processing, involves nucleation and growth. An anti-solvent rapidly removes the solvent from a solution containing perovskite precursors, leading to crystal grain formation. Controlling grain structure is critical for high-efficiency solar cells,^{150,151} yet the impact of grain boundaries remains a topic of debate, with some studies suggesting they extend charge carrier lifetimes¹⁵² and others indicating they promote recombination.¹⁵³

We applied the PI-PM method to methylammonium lead iodide (MAPbI₃), a well-known perovskite material, to investigate the dependency of charge carrier response on its structure. An MAI-rich MAPbI₃ sample was prepared, considering various studies on the optimal PbI₂ and MAI ratios for maximizing PCE. The role of MAI, however, is still debated, with conflicting views on whether it acts as a recombination center or a passivation layer.

Figure 25 displays a sequence of refractive index change images (0 ns – 10 μs) in a MAPbI₃ film using the PI-PM method. The photo-irradiated areas showed contrasting images due to photo-excited charge carriers. Initially, these contrasts strengthened, then gradually faded over several microseconds. We used Fourier transformation to analyze image intensity variations, revealing averaged transient responses. The decay in these responses is attributed to charge carrier recombination. The process occurring in less than 10 nanoseconds is less clear but is thought to involve charge trapping during transport/diffusion, followed by recombination.

Charge carrier behaviors were categorized through clustering analysis.⁸⁶ Figure 26 shows these categorized mappings and average responses, with two groups exhibiting rise-decay curves of varying intensities, indicating differences in photo-excited carrier densities. A third category with little or no response was also identified, typically in areas 5-10 μm in diameter. By overlapping the category map with microscopic film surface images, a clear correlation between surface structure and charge carrier responses was established, with Category 2 representing transitional regions between the other two. This suggests that categories with less or no photo-excited charge carriers occupied some regions.

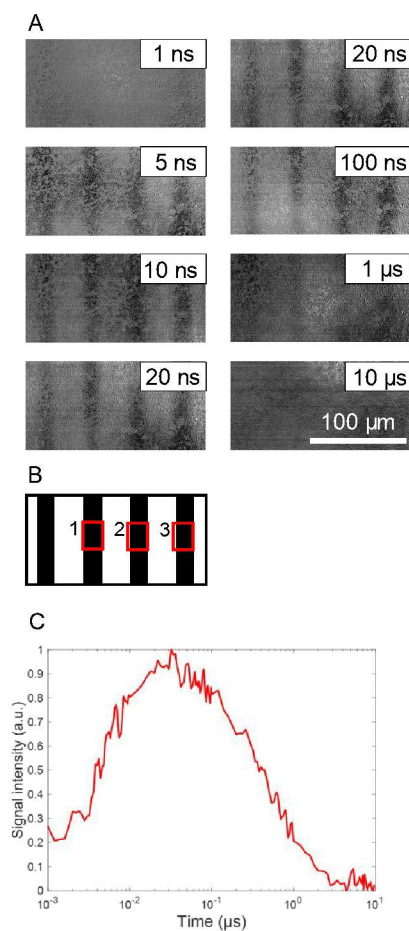


Figure 25 **A**: An image sequence of the refractive index change (0 ns – 10 ms) for a MAPbI₃ film measured by the PI-PM. The scale bar corresponds to 100 μm. **B**: The bottom drawing shows a pump intensity pattern. The red rectangle corresponds to the regions used for the following cluster analyses. **C**: The average transient response obtained from the images in **A**. It was obtained by analyzing the amplitude change of the stripe pattern of the photo-induced refractive index change impinged onto a sample. Reproduced from ref. 82 with permission from American Chemical Society, copyright 2021.

As the proportion of MAI increased, there was a notable rise in the number of local aggregates. Significantly, in these areas, photo-excited charge carriers were not detected within the time frame of nanoseconds to microseconds. This observation suggests that the presence of intermediate species, likely due to increased MAI, could reduce the power conversion efficiency (PCE) of these materials. Our findings imply that MAI might adversely affect this by contributing to the formation of these intermediate species. This supports the conclusion that MAI negatively impacts the generation or transport of charge carriers, as evidenced by a decrease in charge carriers around these MAI-induced

intermediates over periods ranging from nanoseconds to microseconds.

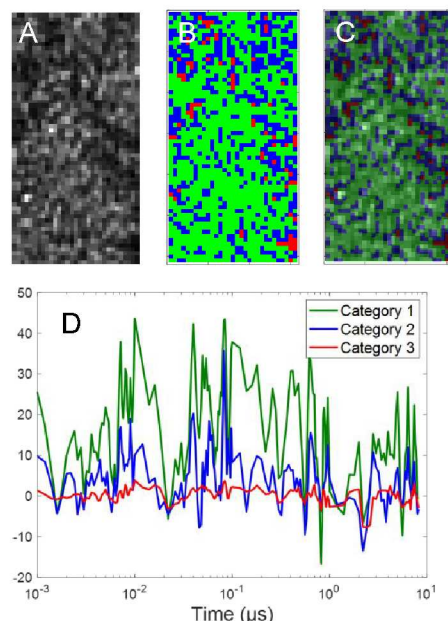


Figure 26 **A**: The categorized mapping of the charge carrier responses in Fig. 1 (Region 2). **B**: A microscopic image at the same area as **A**. **C**: overlapping image of **A** and **B**. **D**: The averaged responses for each categorized response. Reproduced from ref. 82 with permission from American Chemical Society, copyright 2021.

Alongside efforts to enhance perovskite materials, researchers have been exploring the dynamics of charge carriers within the charge-generating perovskite layer and at its interfaces with the electron transport layer (ETL) and hole transport layer (HTL). This research aims to boost efficiency by comprehending how charge carriers are transported and lost during charge extraction. Studies have primarily utilized transient absorption (TA),¹⁵⁴ time-resolved photoluminescence (PL),¹⁵⁵ time-resolved microwave conductivity,^{156,157} and electrical transients^{158,159} to gather insights on these dynamics. However, understanding charge transport to ETLs and HTLs remains somewhat unclear. Measurements from time-resolved PL, TA, and microwave conductivity have shown differing temporal responses for charge transfer.^{160–162}^{156,157}

The electrical transient results have indicated that charge distribution within the perovskite film is established at around 50 ns,¹⁵⁸ attributed to charge transport. Our work supports the notion of charge trapping during diffusion on the nanosecond scale for various photovoltaic and photocatalytic materials. We also examined the microscopic charge transfer at the interfaces between HTLs and perovskite layers for several HTL types using the PI-PM method.¹⁰²

For this study, Spiro-OMeTAD, PTAA, and P3HT were applied as HTLs over MAPbI₃ films.

Figure 27 displays the time responses for both MAPbI₃ alone and HTL/MAPbI₃ composites. The signal from the MAPbI₃ film peaked at around 70 ns before fading over several μ s. In contrast, with Spiro-OMeTAD and PTAA as HTLs, we observed a delay in the initial rise and a deceleration in decay responses, with time constants significantly slower compared to MAPbI₃ alone.

The rising component in MAPbI₃ is associated with the charge-trapping process during internal diffusion within the perovskite layer. Meanwhile, the decay component is linked to Shockley-Read-Hall (SRH) recombination, inferred from the lack of response time dependency on pump intensity.¹⁴⁴ It's hypothesized that during diffusion, charge carriers are trapped at surface states,^{82,102} then transferred to the HTL through the MAPbI₃-HTL interface. This results in reduced signal intensity due to fewer trapped charge carriers at interfacial states, and a subsequent slowdown in accumulation at these states.

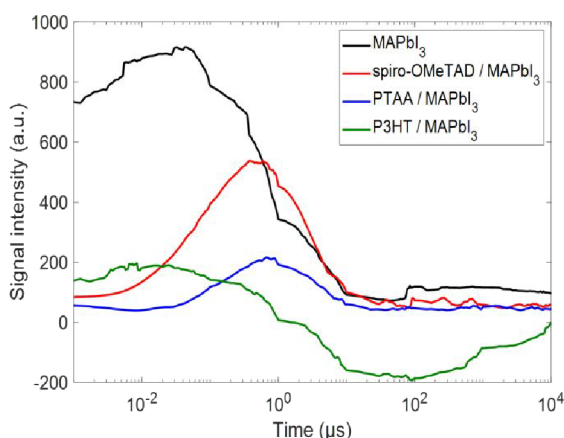


Figure 27 The average transient responses are shown for the spiro-OMeTAD, PTAA, and P3HT/MAPbI₃ and MAPbI₃ only films, which were obtained from the image sequences of the refractive index change measured using the PI-PM method. The signal intensities were obtained by analyzing the amplitudes of the stripe pattern of the photoinduced refractive index change. Reproduced from ref. 137 with permission from American Chemical Society, copyright 2022.

In our observations of the P3HT/MAPbI₃ film, a distinctly different response emerged compared to the MAPbI₃-only film. While the initial few μ s exhibited a positive response similar to MAPbI₃, a longer-lasting negative response, indicative of a refractive index change in the opposite direction, was also noted. This negative response decayed over approximately 10 ms, although the complete decay of the image extended to around 100 m. We attributed this slow, negative response to the transfer of holes to the P3HT layer.

Figure 28 presents the clustering analysis for the P3HT/MAPbI₃ film, revealing three types of responses: a positive response (category 1), a negative response (category 2), and no response (category 3). The positive and negative responses correspond to different types of charge carriers. Category 1 exhibited a rise until 70 ns, followed by decay over several μ s, while Category 2 showed

a rise up until 30 μs , persisting for milliseconds. Based on our analysis, the response in Category 1 is associated with charge carriers in MAPbI_3 , linked to charge trapping and recombination. It's reasonable to infer that the holes were being transferred to the P3HT layer.

Interestingly, the areas exhibiting charge carrier responses in MAPbI_3 and the hole responses in P3HT were spatially distinct at the microscale. Due to this positional difference, the hole response in P3HT was distinctly observed through clustering analysis. It was evident that hole transfer persisted for as long as 10 μs and could endure over milliseconds. Notably, the regions corresponding to Category 2 in Figure 28B did not align with the microscopic image. Unlike other HTL/ MAPbI_3 combinations, the mapping of charge carrier types did not correlate with the film surface morphology of the MAPbI_3 layer. This suggests that the holes were dispersed throughout the P3HT layer, offering a unique insight into the behavior of charge carriers in this material system.

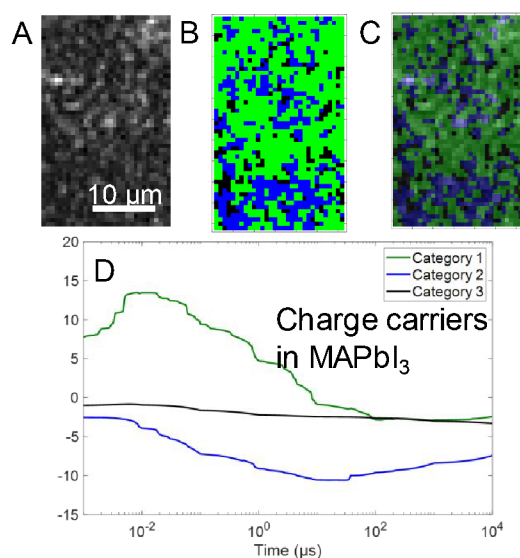


Figure 28 The categorized mapping of the charge carrier responses of P3HT / MAPbI_3 . **A** corresponds to a microscopic image and the corresponding categorized map is shown in **B**. **C** is an image of the overlap between **A** and **B**. The averaged responses for three categories are shown in **D**. Reproduced from ref. 137 with permission from American Chemical Society, copyright 2022.

Using the PI-PM method, we were able to discern the dynamics of photo-excited charge carriers in various HTL/ MAPbI_3 film combinations. This method's ability to microscopically differentiate revealed that in films using spiro-OMeTAD and PTAA as HTLs, hole dynamics closely followed the local structure of the MAPbI_3 layer. Conversely, in the P3HT/ MAPbI_3 combination, the transferred holes were more widely distributed. This indicates that in the former HTLs, the holes tended to be localized near the MAPbI_3 layer, whereas in P3HT, the holes demonstrated greater mobility, moving

freely within the layer. This characteristic of long-lasting, mobile holes in P3HT may offer advantages for enhanced photoconversion efficiency compared to other HTLs.

4. Conclusion

Pattern-illumination time-resolved phase microscopy (PI-PM) is a technique used to study the dynamics of photo-excited charge carriers in materials. It involves illuminating a sample with an arbitrary light pattern and imaging the refractive index change caused by the photo-excited charge carriers using phase-contrast imaging. The PI-PM method provides information on the charge carrier dynamics with a high time resolution and can differentiate between different types of charge carriers. It has been applied to study various photocatalytic materials such as TiO_2 , Fe_2O_3 , SrTiO_3 and BiVO_4 films. The method is particularly useful for studying particulate semiconductor films, where the charge carrier dynamics differ from those in single crystals. PI-PM allows for the observation of non-radiative processes such as charge trapping and interfacial charge transfer, which are not easily detected by other time-resolved methods. This technique provides valuable insights into the optimization of photovoltaic and photocatalytic substrates, especially for understanding the active/inactive sites of the photo-devices.

Author contribution Statement

KK wrote and reviewed the manuscript.

Competing interests

I declare that the authors have no competing interests or other interests that might be perceived to influence the results and/or discussion reported in this article.

Acknowledgements

The research was financially supported by JSPS Kakenhi (#22K05158), Iketani Science and Technology Foundation, JST PRESTO (#JPMJPR1675) and the Institute of Science and Engineering, Chuo University.

References

- 1 A. Hagfeldt, G. Boschloo, L. C. Sun, L. Kloo and H. Pettersson, Dye-Sensitized Solar Cells, *Chem. Rev.*, 2010, **110**, 6595–6663.
- 2 L. K. Ono, E. J. Juarez-Perez and Y. Qi, Progress on Perovskite Materials and Solar Cells with Mixed Cations and Halide Anions, *ACS Appl. Mater. Interfaces*, 2017, **9**, 30197–30246.
- 3 A. Kojima, K. Teshima, Y. Shirai and T. Miyasaka, Organometal Halide Perovskites as Visible-Light Sensitizers for Photovoltaic Cells, *J. Am. Chem. Soc.*, 2009, **131**, 6050–6051.
- 4 M. I. H. Ansari, A. Qurashi and M. K. Nazeeruddin, Frontiers, opportunities, and challenges in perovskite solar cells: A critical review, *J. Photochem. Photobiol. C Photochem. Rev.*, 2018, **35**, 1–24.
- 5 W.-J. Yin, J.-H. Yang, J. Kang, Y. Yan and S.-H. Wei, Halide perovskite materials for solar cells: a theoretical review, *J. Mater. Chem. A*, 2015, **3**, 8926–8942.
- 6 G. Niu, X. Guo and L. Wang, Review of recent progress in chemical stability of perovskite solar cells, *J. Mater. Chem. A*, 2015, **3**, 8970–8980.
- 7 H. Anwar, I. Arif, U. Javeed, H. Mushtaq, K. Ali and S. K. Sharma, in *Solar Cells: From Materials to Device Technology*, eds. S. K. Sharma and K. Ali, Springer International Publishing, Cham, 2020, pp. 235–258.
- 8 J. Gong, K. Sumathy, Q. Qiao and Z. Zhou, Review on dye-sensitized solar cells (DSSCs): Advanced techniques and research trends, *Renew. Sustain. Energy Rev.*, 2017, **68**, 234–246.
- 9 M. Grätzel, Dye-sensitized solar cells, *J. Photochem. Photobiol. C Photochem. Rev.*, 2003, **4**, 145–153.
- 10 D. Friedmann, A. Hakki, H. Kim, W. Choi and D. Bahnemann, Heterogeneous photocatalytic organic synthesis: state-of-the-art and future perspectives, *Green Chem.*, 2016, **18**, 5391–5411.
- 11 J. Schneider, M. Matsuoka, M. Takeuchi, J. Zhang, Y. Horiuchi, M. Anpo and D. W. Bahnemann, Understanding TiO₂ Photocatalysis: Mechanisms and Materials, *Chem. Rev.*, 2014, **114**, 9919–9986.
- 12 D. Sudha and P. Sivakumar, Review on the photocatalytic activity of various composite catalysts, *Chem. Eng. Process. Process Intensif.*, 2015, **97**, 112–133.
- 13 S. Chen, T. Takata and K. Domen, Particulate photocatalysts for overall water splitting, *Nat. Rev. Mater.*, 2017, **2**, 17050.
- 14 A. G. Tamirat, J. Rick, A. A. Dubale, W.-N. Su and B.-J. Hwang, Using hematite for photoelectrochemical water splitting: a review of current progress and challenges, *Nanoscale Horiz.*, 2016, **1**, 243–267.
- 15 Y. Lin, G. Yuan, S. Sheehan, S. Zhou and D. Wang, Hematite-based solar water splitting: challenges and opportunities, *Energy Environ. Sci.*, 2011, **4**, 4862–4869.

- 16 K. Maeda, Photocatalytic water splitting using semiconductor particles: History and recent developments, *J. Photochem. Photobiol. C Photochem. Rev.*, 2011, **12**, 237–268.
- 17 Z. Wang, C. Li and K. Domen, Recent developments in heterogeneous photocatalysts for solar-driven overall water splitting, *Chem. Soc. Rev.*, 2019, **48**, 2109–2125.
- 18 N. Serpone and A. V. Emeline, Semiconductor Photocatalysis — Past, Present, and Future Outlook, *J. Phys. Chem. Lett.*, 2012, **3**, 673–677.
- 19 F. Wang, Q. Li and D. Xu, Recent Progress in Semiconductor-Based Nanocomposite Photocatalysts for Solar-to-Chemical Energy Conversion, *Adv. Energy Mater.*, 2017, **7**, 1700529.
- 20 R. Qian, H. Zong, J. Schneider, G. Zhou, T. Zhao, Y. Li, J. Yang, D. W. Bahnemann and J. H. Pan, Charge carrier trapping, recombination and transfer during TiO₂ photocatalysis: An overview, *Catal. Today*, 2019, **335**, 78–90.
- 21 Q. Wang, S. Okunaka, H. Tokudome, T. Hisatomi, M. Nakabayashi, N. Shibata, T. Yamada and K. Domen, Printable Photocatalyst Sheets Incorporating a Transparent Conductive Mediator for Z-Scheme Water Splitting, *Joule*, 2018, **2**, 2667–2680.
- 22 A. Yamakata, T. Ishibashi and H. Onishi, Time-resolved infrared absorption spectroscopy of photogenerated electrons in platinized TiO₂ particles, *Chem. Phys. Lett.*, 2001, **333**, 271–277.
- 23 A. Yamakata and J. J. M. Vequizo, Curious behaviors of photogenerated electrons and holes at the defects on anatase, rutile, and brookite TiO₂ powders: A review, *J. Photochem. Photobiol. C Photochem. Rev.*, 2018, **40**, 234–243.
- 24 J. J. M. Vequizo, H. Matsunaga, T. Ishiku, S. Kamimura, T. Ohno and A. Yamakata, Trapping-Induced Enhancement of Photocatalytic Activity on Brookite TiO₂ Powders: Comparison with Anatase and Rutile TiO₂ Powders, *ACS Catal.*, 2017, **7**, 2644–2651.
- 25 M. Ebihara, W. Y. Sohn and K. Katayama, Lifetime mapping of photo-excited charge carriers by the transient grating imaging technique for nano-particulate semiconductor films, *Rev. Sci. Instrum.*, 2019, **90**, 073905.
- 26 A. Yamakata, M. Kawaguchi, R. Murachi, M. Okawa and I. Kamiya, Dynamics of Photogenerated Charge Carriers on Ni- and Ta-Doped SrTiO₃ Photocatalysts Studied by Time-Resolved Absorption and Emission Spectroscopy, *J. Phys. Chem. C*, 2016, **120**, 7997–8004.
- 27 A. Yamakata, J. J. M. Vequizo and M. Kawaguchi, Behavior and Energy State of Photogenerated Charge Carriers in Single-Crystalline and Polycrystalline Powder SrTiO₃ Studied by Time-Resolved Absorption Spectroscopy in the Visible to Mid-Infrared Region, *J. Phys. Chem. C*, 2015, **119**, 1880–1885.
- 28 S. Selim, E. Pastor, M. García-Tecedor, M. R. Morris, L. Francàs, M. Sachs, B. Moss, S. Corby, C. A. Mesa, S. Gimenez, A. Kafizas, A. A. Bakulin and J. R. Durrant, Impact of Oxygen Vacancy Occupancy on Charge Carrier Dynamics in BiVO₄ Photoanodes, *J. Am. Chem. Soc.*, 2019, **141**, 18791–18798.

- 29 M. Sachs, J.-S. Park, E. Pastor, A. Kafizas, A. A. Wilson, L. Francàs, S. Gul, M. Ling, C. Blackman, J. Yano, A. Walsh and J. R. Durrant, Effect of oxygen deficiency on the excited state kinetics of WO₃ and implications for photocatalysis, *Chem. Sci.*, 2019, **10**, 5667–5677.
- 30 C. A. Mesa, L. Francàs, K. R. Yang, P. Garrido-Barros, E. Pastor, Y. Ma, A. Kafizas, T. E. Rosser, M. T. Mayer, E. Reisner, M. Grätzel, V. S. Batista and J. R. Durrant, Multihole water oxidation catalysis on haematite photoanodes revealed by operando spectroelectrochemistry and DFT, *Nat. Chem.*, 2019, **12**, 82–89.
- 31 W. Y. Sohn, M. Inaba, T. Tokubuchi, J. E. Thorne, D. Wang and K. Katayama, Uncovering Photo-Excited Charge Carrier Dynamics in Hematite (α -Fe₂O₃) Hidden in the Nanosecond Range by the Heterodyne Transient Grating Technique Combined with the Randomly Interleaved Pulse-Train Method, *J. Phys. Chem. C*, 2019, **123**, 6693–6700.
- 32 W. Y. Sohn, J. E. Thorne, Y. Zhang, S. Kuwahara, Q. Shen, D. Wang and K. Katayama, Charge carrier kinetics in hematite with NiFeO_x coating in aqueous solutions: Dependence on bias voltage, *J. Photochem. Photobiol. Chem.*, 2018, **353**, 344–348.
- 33 Y. Yamada and Y. Kanemitsu, Determination of electron and hole lifetimes of rutile and anatase TiO₂ single crystals, *Appl. Phys. Lett.*, 2012, **101**, 133907.
- 34 A. J. Cowan, J. Tang, W. Leng, J. R. Durrant and D. R. Klug, Water Splitting by Nanocrystalline TiO₂ in a Complete Photoelectrochemical Cell Exhibits Efficiencies Limited by Charge Recombination, *J. Phys. Chem. C*, 2010, **114**, 4208–4214.
- 35 Y. Tamaki, A. Furube, M. Murai, K. Hara, R. Katoh and M. Tachiya, Dynamics of efficient electron–hole separation in TiO₂ nanoparticles revealed by femtosecond transient absorption spectroscopy under the weak-excitation condition, *Phys. Chem. Chem. Phys.*, 2007, **9**, 1453–1460.
- 36 A. Yamakata, T. Ishibashi and H. Onishi, Water- and Oxygen-Induced Decay Kinetics of Photogenerated Electrons in TiO₂ and Pt/TiO₂: A Time-Resolved Infrared Absorption Study, *J. Phys. Chem. B*, 2001, **105**, 7258–7262.
- 37 A. Yamakata, T. Ishibashi and H. Onishi, Electron- and Hole-Capture Reactions on Pt/TiO₂ Photocatalyst Exposed to Methanol Vapor Studied with Time-Resolved Infrared Absorption Spectroscopy, *J. Phys. Chem. B*, 2002, **106**, 9122–9125.
- 38 A. Y. Anderson, P. R. F. Barnes, J. R. Durrant and B. C. O'Regan, Simultaneous Transient Absorption and Transient Electrical Measurements on Operating Dye-Sensitized Solar Cells: Elucidating the Intermediates in Iodide Oxidation, *J. Phys. Chem. C*, 2010, **114**, 1953–1958.
- 39 M. Barroso, S. R. Pendlebury, A. J. Cowan and J. R. Durrant, Charge carrier trapping, recombination and transfer in hematite (α -Fe₂O₃) water splitting photoanodes, *Chem. Sci.*, 2013, **4**, 2724–2734.
- 40 R. Brüninghoff, K. Wenderich, J. P. Kortarik, B. T. Mei, G. Mul and A. Huijser, Time-Dependent Photoluminescence of Nanostructured Anatase TiO₂ and the Role of Bulk and Surface Processes,

- J. Phys. Chem. C*, 2019, **123**, 26653–26661.
- 41 M. Gallart, T. Cottineau, B. Hönerlage, V. Keller, N. Keller and P. Gilliot, Temperature dependent photoluminescence of anatase and rutile TiO₂ single crystals: Polaron and self-trapped exciton formation, *J. Appl. Phys.*, 2018, **124**, 133104.
- 42 C. P. Saini, A. Barman, D. Banerjee, O. Grynko, S. Prucnal, M. Gupta, D. M. Phase, A. K. Sinha, D. Kanjilal, W. Skorupa and A. Kanjilal, Impact of Self-Trapped Excitons on Blue Photoluminescence in TiO₂ Nanorods on Chemically Etched Si Pyramids, *J. Phys. Chem. C*, 2017, **121**, 11448–11454.
- 43 M. K. Singh and M. S. Mehata, Temperature-dependent photoluminescence and decay times of different phases of grown TiO₂ nanoparticles: Carrier dynamics and trap states, *Ceram. Int.*, , DOI:10.1016/j.ceramint.2021.08.147.
- 44 D. Wei, Y. Huang, J. Bai and H. J. Seo, Manipulating Luminescence and Photocatalytic Activities of BiVO₄ by Eu³⁺ Ions Incorporation, *J. Phys. Chem. C*, 2020, **124**, 11767–11779.
- 45 X. Wang, S. Shen, Z. Feng and C. Li, Time-resolved photoluminescence of anatase/rutile TiO₂ phase junction revealing charge separation dynamics, *Chin. J. Catal.*, 2016, **37**, 2059–2068.
- 46 S. Qin, N. Denisov, X. Zhou, L. Zdražil, D. Fehn, I. Hwang, M. Bruns, H. Kim, K. Meyer and P. Schmuki, Critical factors for photoelectrochemical and photocatalytic H₂ evolution from grey anatase (001) nanosheets, *J. Phys. Energy*, , DOI:10.1088/2515-7655/ac8ed3.
- 47 F. Ichihara, F. Sieland, H. Pang, D. Philo, A.-T. Duong, K. Chang, T. Kako, D. W. Bahnemann and J. Ye, Photogenerated Charge Carriers Dynamics on La- and/or Cr-Doped SrTiO₃ Nanoparticles Studied by Transient Absorption Spectroscopy, *J. Phys. Chem. C*, 2020, **124**, 1292–1302.
- 48 S. Selim, L. Francàs, M. García-Tecedor, S. Corby, C. Blackman, S. Gimenez, J. R. Durrant and A. Kafizas, WO₃/BiVO₄: impact of charge separation at the timescale of water oxidation, *Chem. Sci.*, 2019, **10**, 2643–2652.
- 49 I. Grigioni, L. Ganzer, F. V. A. Camargo, B. Bozzini, G. Cerullo and E. Selli, In Operando Photoelectrochemical Femtosecond Transient Absorption Spectroscopy of WO₃/BiVO₄ Heterojunctions, *ACS Energy Lett.*, 2019, **4**, 2213–2219.
- 50 J. Ravensbergen, F. F. Abdi, J. H. van Santen, R. N. Frese, B. Dam, R. van de Krol and J. T. M. Kennis, Unraveling the Carrier Dynamics of BiVO₄: A Femtosecond to Microsecond Transient Absorption Study, *J. Phys. Chem. C*, 2014, **118**, 27793–27800.
- 51 S. A. J. Hillman, R. S. Sprick, D. Pearce, D. J. Woods, W.-Y. Sit, X. Shi, A. I. Cooper, J. R. Durrant and J. Nelson, Why Do Sulfone-Containing Polymer Photocatalysts Work So Well for Sacrificial Hydrogen Evolution from Water?, *J. Am. Chem. Soc.*, 2022, **144**, 19382–19395.
- 52 H. Zhu, S. Xiao, W. Tu, S. Yan, T. He, X. Zhu, Y. Yao, Y. Zhou and Z. Zou, In Situ Determination of Polaron-Mediated Ultrafast Electron Trapping in Rutile TiO₂ Nanorod Photoanodes, *J. Phys.*

- Chem. Lett.*, 2021, 10815–10822.
- 53 Y. Li, Q. Wu, Y. Chen, R. Zhang, C. Li, K. Zhang, M. Li, Y. Lin, D. Wang, X. Zou and T. Xie, Interface engineering Z-scheme Ti-Fe₂O₃/In₂O₃ photoanode for highly efficient photoelectrochemical water splitting, *Appl. Catal. B Environ.*, 2021, **290**, 120058.
- 54 Y. Yamada, H. Yasuda, T. Tayagaki and Y. Kanemitsu, Photocarrier recombination dynamics in highly excited SrTiO₃ studied by transient absorption and photoluminescence spectroscopy, *Appl. Phys. Lett.*, 2009, **95**, 121112.
- 55 M. M. Gabriel, J. R. Kirschbrown, J. D. Christesen, C. W. Pinion, D. F. Zigler, E. M. Grumstrup, B. P. Mehl, E. E. M. Cating, J. F. Cahoon and J. M. Papanikolas, Direct Imaging of Free Carrier and Trap Carrier Motion in Silicon Nanowires by Spatially-Separated Femtosecond Pump-Probe Microscopy, *Nano Lett.*, 2013, **13**, 1336–1340.
- 56 T. Zhu, L. Yuan, Y. Zhao, M. Zhou, Y. Wan, J. Mei and L. Huang, Highly mobile charge-transfer excitons in two-dimensional WS₂/tetracene heterostructures, *Sci. Adv.*, 2018, **4**, eaao3104.
- 57 Z. Guo, Y. Wan, M. Yang, J. Snaider, K. Zhu and L. Huang, Long-range hot-carrier transport in hybrid perovskites visualized by ultrafast microscopy, *Science*, 2017, **356**, 59–62.
- 58 M. C. Fischer, J. W. Wilson, F. E. Robles and W. S. Warren, Invited Review Article: Pump-probe microscopy, *Rev. Sci. Instrum.*, 2016, **87**, 031101.
- 59 M. C. Fravventura, L. D. A. Siebbeles and T. J. Savenije, Mechanisms of Photogeneration and Relaxation of Excitons and Mobile Carriers in Anatase TiO₂, *J. Phys. Chem. C*, 2014, **118**, 7337–7343.
- 60 M. Ziwrtsch, S. Müller, H. Hempel, T. Unold, F. F. Abdi, R. van de Krol, D. Friedrich and R. Eichberger, Direct Time-Resolved Observation of Carrier Trapping and Polaron Conductivity in BiVO₄, *ACS Energy Lett.*, 2016, **1**, 888–894.
- 61 S. Kuwahara and K. Katayama, Distinction of electron pathways at titanium oxide/liquid interfaces in photocatalytic processes and co-catalyst effects, *Phys. Chem. Chem. Phys.*, 2016, **18**, 25271–25276.
- 62 S. Kuwahara, H. Hata, S. Taya, N. Maeda, Q. Shen, T. Toyoda and K. Katayama, Detection of non-absorbing charge dynamics via refractive index change in dye-sensitized solar cells, *Phys. Chem. Chem. Phys.*, 2013, **15**, 5975–5981.
- 63 Y. Zhu and J.-X. Cheng, Transient absorption microscopy: Technological innovations and applications in materials science and life science, *J. Chem. Phys.*, 2020, **152**, 020901.
- 64 Z. Guo, J. S. Manser, Y. Wan, P. V. Kamat and L. Huang, Spatial and temporal imaging of long-range charge transport in perovskite thin films by ultrafast microscopy, *Nat. Commun.*, 2015, **6**, 7471.
- 65 L. Yuan, T.-F. Chung, A. Kuc, Y. Wan, Y. Xu, Y. P. Chen, T. Heine and L. Huang, Photocarrier generation from interlayer charge-transfer transitions in WS₂-graphene heterostructures, *Sci. Adv.*,

- 2018, **4**, e1700324.
- 66 S. J. Yoon, Z. Guo, P. C. dos Santos Claro, E. V. Shevchenko and L. Huang, Direct Imaging of Long-Range Exciton Transport in Quantum Dot Superlattices by Ultrafast Microscopy, *ACS Nano*, 2016, **10**, 7208–7215.
- 67 G. G. Rozenman, K. Akulov, A. Golombek and T. Schwartz, Long-Range Transport of Organic Exciton-Polaritons Revealed by Ultrafast Microscopy, *ACS Photonics*, 2018, **5**, 105–110.
- 68 P. Wang, M. N. Slipchenko, J. Mitchell, C. Yang, E. O. Potma, X. Xu and J.-X. Cheng, Far-field imaging of non-fluorescent species with subdiffraction resolution, *Nat. Photonics*, 2013, **7**, 449–453.
- 69 Y.-H. Kim and P. T. C. So, Three-dimensional wide-field pump-probe structured illumination microscopy, *Opt. Express*, 2017, **25**, 7369–7391.
- 70 E. S. Massaro, A. H. Hill and E. M. Grumstrup, Super-Resolution Structured Pump–Probe Microscopy, *ACS Photonics*, 2016, **3**, 501–506.
- 71 M. J. Simpson, B. Doughty, B. Yang, K. Xiao and Y.-Z. Ma, Imaging Electronic Trap States in Perovskite Thin Films with Combined Fluorescence and Femtosecond Transient Absorption Microscopy, *J. Phys. Chem. Lett.*, 2016, **7**, 1725–1731.
- 72 A. M. El-Zohry, B. S. Shaheen, V. M. Burlakov, J. Yin, M. N. Hedhili, S. Shikin, B. Ooi, O. M. Bakr and O. F. Mohammed, Extraordinary Carrier Diffusion on CdTe Surfaces Uncovered by 4D Electron Microscopy, *Chem*, DOI:10.1016/j.chempr.2018.12.020.
- 73 R. Bose, J. Sun, J. I. Khan, B. S. Shaheen, A. Adhikari, T. K. Ng, V. M. Burlakov, M. R. Parida, D. Priante, A. Goriely, B. S. Ooi, O. M. Bakr and O. F. Mohammed, Real-Space Visualization of Energy Loss and Carrier Diffusion in a Semiconductor Nanowire Array Using 4D Electron Microscopy, *Adv. Mater.*, 2016, **28**, 5106–5111.
- 74 A. Yurtsever and A. H. Zewail, 4D Nanoscale Diffraction Observed by Convergent-Beam Ultrafast Electron Microscopy, *Science*, 2009, **326**, 708.
- 75 J. Cho, T. Y. Hwang and A. H. Zewail, Visualization of carrier dynamics in p(n)-type GaAs by scanning ultrafast electron microscopy, *Proc. Natl. Acad. Sci.*, 2014, **111**, 2094.
- 76 J. Sun, A. Adhikari, B. S. Shaheen, H. Yang and O. F. Mohammed, Mapping Carrier Dynamics on Material Surfaces in Space and Time using Scanning Ultrafast Electron Microscopy, *J. Phys. Chem. Lett.*, 2016, **7**, 985–994.
- 77 N. Maeda, H. Hata, N. Osada, Q. Shen, T. Toyoda, S. Kuwahara and K. Katayama, Carrier dynamics in quantum-dot sensitized solar cells measured by transient grating and transient absorption methods, *Phys. Chem. Chem. Phys.*, 2013, **15**, 11006–11013.
- 78 S. Kuwahara, H. Hata, S. Taya, N. Maeda, Q. Shen, T. Toyoda and K. Katayama, Detection of non-absorbing charge dynamics via refractive index change in dye-sensitized solar cells, *Phys. Chem. Chem. Phys.*, 2013, **15**, 5975–5981.

- 79 K. Katayama, M. Yamaguchi and T. Sawada, Lens-free heterodyne detection for transient grating experiments, *Appl. Phys. Lett.*, 2003, **82**, 2775–2777.
- 80 M. Okuda and K. Katayama, Selective detection of real and imaginary parts of refractive index change in solutions induced by photoexcitation using near-field heterodyne transient grating method, *Chem. Phys. Lett.*, 2007, **443**, 158–162.
- 81 P. J. Steinbach, R. Ionescu and C. R. Matthews, Analysis of kinetics using a hybrid maximum-entropy/nonlinear-least-squares method: Application to protein folding, *Biophys. J.*, 2002, **82**, 2244–2255.
- 82 T. Chugenji, M. Ebihara and K. Katayama, Charge Carrier Inhomogeneity of MAPbI₃ Clarified by the Clustering of the Time-Resolved Microscopic Image Sequence, *ACS Appl. Energy Mater.*, 2021, **4**, 6430–6435.
- 83 N. Osada, T. Oshima, S. Kuwahara, T. Toyoda, Q. Shen and K. Katayama, Photoexcited carrier dynamics of double-layered CdS/CdSe quantum dot sensitized solar cells measured by heterodyne transient grating and transient absorption methods, *Phys. Chem. Chem. Phys.*, 2014, **16**, 5774–5778.
- 84 D. Shingai, Y. Ide, W. Y. Sohn and K. Katayama, Photoexcited charge carrier dynamics of interconnected TiO₂ nanoparticles: evidence of enhancement of charge separation at anatase–rutile particle interfaces, *Phys. Chem. Chem. Phys.*, 2018, **20**, 3484–3489.
- 85 K. Katayama, Photo-excited charge carrier imaging by time-resolved pattern illumination phase microscopy, *J. Chem. Phys.*, 2020, **153**, 054201.
- 86 M. Ebihara and K. Katayama, Anomalous Charge Carrier Decay Spotted by Clustering of a Time-Resolved Microscopic Phase Image Sequence, *J. Phys. Chem. C*, 2020, **124**, 23551–23557.
- 87 M. Ebihara, T. Ikeda, S. Okunaka, H. Tokudome, K. Domen and K. Katayama, Charge carrier mapping for Z-scheme photocatalytic water-splitting sheet via categorization of microscopic time-resolved image sequences, *Nat. Commun.*, 2021, **12**, 3716.
- 88 K. Katayama, D. Kato, K.-I. Nagasaka, M. Miyagawa, W. Y. Sohn and K.-W. Lee, Origin of optical nonlinearity of photo-responsive liquid crystals revealed by transient grating imaging, *Sci. Rep.*, 2019, **9**, 5754.
- 89 R. M. Koehl, S. Adachi and K. A. Nelson, Direct Visualization of Collective Wavepacket Dynamics, *J. Phys. Chem. A*, 1999, **103**, 10260–10267.
- 90 K. Katayama, T. Chugenji and K. Kawaguchi, Defocus-induced phase contrast enhancement in pattern illumination time-resolved phase microscopy, *AIP Adv.*, 2021, **11**, 115215.
- 91 C. S. K. Ranasinghe and A. Yamakata, Structural changes of water molecules during photoelectrochemical water oxidation on TiO₂ thin film electrodes, *Phys. Chem. Chem. Phys.*, , DOI:10.1039/C7CP06646E.
- 92 N. Georges T, A. Rola and W. Logan, *Analog and Digital Holography with MATLAB*, SPIE, Washington, DC, 2015.

- 93 S. Ono, T. Miyata and I. Yamada, Cartoon-Texture Image Decomposition Using Blockwise Low-Rank Texture Characterization, *IEEE Trans. Image Process.*, 2014, **23**, 1128–1142.
- 94 E. J. Candès, X. Li, Y. Ma and J. Wright, Robust principal component analysis?, *J. ACM*, 2011, **58**, 11:1-11:37.
- 95 J. Wright, A. Ganesh, S. Rao, Y. Peng and Y. Ma, in *Advances in Neural Information Processing Systems 22*, eds. Y. Bengio, D. Schuurmans, J. D. Lafferty, C. K. I. Williams and A. Culotta, Curran Associates, Inc., 2009, pp. 2080–2088.
- 96 M. Ozaki, A. Shimazaki, M. Jung, Y. Nakaike, N. Maruyama, S. Yakumar, A. I. Rafieh, T. Sasamori, N. Tokitoh, P. Ekanayake, Y. Murata, R. Murdey and A. Wakamiya, A Purified, Solvent-Intercalated Precursor Complex for Wide-Process-Window Fabrication of Efficient Perovskite Solar Cells and Modules, *Angew. Chem. Int. Ed.*, 2019, **58**, 9389–9393.
- 97 E. H. Jung, N. J. Jeon, E. Y. Park, C. S. Moon, T. J. Shin, T.-Y. Yang, J. H. Noh and J. Seo, Efficient, stable and scalable perovskite solar cells using poly(3-hexylthiophene), *Nature*, 2019, **567**, 511–515.
- 98 Q. Zhao, R. Wu, Z. Zhang, J. Xiong, Z. He, B. Fan, Z. Dai, B. Yang, X. Xue, P. Cai, S. Zhan, X. Zhang and J. Zhang, Achieving efficient inverted planar perovskite solar cells with nondoped PTAA as a hole transport layer, *Org. Electron.*, 2019, **71**, 106–112.
- 99 H. Taherianfard, G.-W. Kim, F. Ebadi, T. Abzieher, K. Choi, U. W. Paetzold, B. S. Richards, A. Alrhmman Eliwi, F. Tajabadi, N. Taghavinia and M. Malekshahi Byranvand, Perovskite/Hole Transport Layer Interface Improvement by Solvent Engineering of Spiro-OMeTAD Precursor Solution, *ACS Appl. Mater. Interfaces*, 2019, **11**, 44802–44810.
- 100 K. Katayama, Y. Takeda, K. Shimaoka, K. Yoshida, R. Shimizu, T. Ishiwata, A. Nakamura, S. Kuwahara, A. Mase, T. Sugita and M. Mori, Novel method of screening the oxidation and reduction abilities of photocatalytic materials, *Analyst*, 2014, **139**, 1953–1959.
- 101 H. Hata, K. Katayama, Q. Shen and T. Toyoda, Characterization of Photoexcited Carriers and Thermal Properties of Nanoparticulate TiO₂ Film Using Heterodyne Transient Grating Method, *Jpn. J. Appl. Phys.*, , DOI:10.1143/jjap.51.042601.
- 102 K. Katayama, T. Chugenji and K. Kawaguchi, Charge Carrier Trapping during Diffusion Generally Observed for Particulate Photocatalytic Films, *Energies*, 2021, **14**, 7011.
- 103 K. Kato and A. Yamakata, Defect-Induced Acceleration and Deceleration of Photocarrier Recombination in SrTiO₃ Powders, *J. Phys. Chem. C*, 2020, **124**, 11057–11063.
- 104 K. Furuhashi, Q. Jia, A. Kudo and H. Onishi, Time-Resolved Infrared Absorption Study of SrTiO₃ Photocatalysts Codoped with Rhodium and Antimony, *J. Phys. Chem. C*, 2013, **117**, 19101–19106.
- 105 K. Kato, J. Jiang, Y. Sakata and A. Yamakata, Effect of Na-Doping on Electron Decay Kinetics in SrTiO₃ Photocatalyst, *ChemCatChem*, 2019, **11**, 6349–6354.

- 106 J. J. M. Vequizo, S. Kamimura, T. Ohno and A. Yamakata, Oxygen induced enhancement of NIR emission in brookite TiO₂ powders: comparison with rutile and anatase TiO₂ powders, *Phys. Chem. Chem. Phys.*, DOI:10.1039/C7CP06975H.
- 107 T. Tanaka, A. Harata and T. Sawada, Subpicosecond surface-restricted carrier and thermal dynamics by transient reflectivity measurements, *J. Appl. Phys.*, 1997, **82**, 4033–4038.
- 108 H. Haario, M. Laine, A. Mira and E. Saksman, DRAM: Efficient adaptive MCMC, *Stat. Comput.*, 2006, **16**, 339–354.
- 109 K. Katayama, K. Kawaguchi, Y. Egawa and Z. Pan, Local Charge Carrier Dynamics for Photocatalytic Materials Using Pattern-Illumination Time-Resolved Phase Microscopy, *Energies*, 2022, **15**, 9578.
- 110 X. Huang, J. Fan, L. Li, H. Liu, R. Wu, Y. Wu, L. Wei, H. Mao, A. Lal, P. Xi, L. Tang, Y. Zhang, Y. Liu, S. Tan and L. Chen, Fast, long-term, super-resolution imaging with Hessian structured illumination microscopy, *Nat. Biotechnol.*, 2018, **36**, 451–459.
- 111 K. Kawaguchi, T. Chugenji, S. Okunaka, H. Tokudome and K. Katayama, Distinction and Separation of Different Types of Charge Carriers from the Time-Resolved Local Charge Carrier Mapping for Photocatalytic Materials, *J. Phys. Chem. C*, 2022, **126**, 6646–6652.
- 112 N. Aiga, Q. Jia, K. Watanabe, A. Kudo, T. Sugimoto and Y. Matsumoto, Electron–Phonon Coupling Dynamics at Oxygen Evolution Sites of Visible-Light-Driven Photocatalyst: Bismuth Vanadate, *J. Phys. Chem. C*, 2013, **117**, 9881–9886.
- 113 Y. Suzuki, D. H. K. Murthy, H. Matsuzaki, A. Furube, Q. Wang, T. Hisatomi, K. Domen and K. Seki, Rational Interpretation of Correlated Kinetics of Mobile and Trapped Charge Carriers: Analysis of Ultrafast Carrier Dynamics in BiVO₄, *J. Phys. Chem. C*, 2017, **121**, 19044–19052.
- 114 Q. Wang and K. Domen, Particulate Photocatalysts for Light-Driven Water Splitting: Mechanisms, Challenges, and Design Strategies, *Chem. Rev.*, 2020, **120**, 919–985.
- 115 A. B. Djurišić, Y. He and A. M. C. Ng, Visible-light photocatalysts: Prospects and challenges, *APL Mater.*, 2020, **8**, 030903.
- 116 T. Hisatomi and K. Domen, Reaction systems for solar hydrogen production via water splitting with particulate semiconductor photocatalysts, *Nat. Catal.*, 2019, **2**, 387–399.
- 117 Y. Goto, T. Hisatomi, Q. Wang, T. Higashi, K. Ishikiriyama, T. Maeda, Y. Sakata, S. Okunaka, H. Tokudome, M. Katayama, S. Akiyama, H. Nishiyama, Y. Inoue, T. Takewaki, T. Setoyama, T. Minegishi, T. Takata, T. Yamada and K. Domen, A Particulate Photocatalyst Water-Splitting Panel for Large-Scale Solar Hydrogen Generation, *Joule*, 2018, **2**, 509–520.
- 118 K. Maeda, Z-Scheme Water Splitting Using Two Different Semiconductor Photocatalysts, *ACS Catal.*, 2013, **3**, 1486–1503.
- 119 R. Abe, K. Sayama, K. Domen and H. Arakawa, A new type of water splitting system composed of two different TiO₂ photocatalysts (anatase, rutile) and a IO₃⁻/I⁻ shuttle redox mediator, *Chem.*

- Phys. Lett.*, 2001, **344**, 339–344.
- 120 B.-J. Ng, L. K. Putri, X. Y. Kong, Y. W. Teh, P. Pasbakhsh and S.-P. Chai, Z-Scheme Photocatalytic Systems for Solar Water Splitting, *Adv. Sci.*, 2020, **7**, 1903171.
- 121 Q. Wang, T. Hisatomi, Q. Jia, H. Tokudome, M. Zhong, C. Wang, Z. Pan, T. Takata, M. Nakabayashi, N. Shibata, Y. Li, I. D. Sharp, A. Kudo, T. Yamada and K. Domen, Scalable water splitting on particulate photocatalyst sheets with a solar-to-hydrogen energy conversion efficiency exceeding 1%, *Nat. Mater.*, 2016, **15**, 611–615.
- 122 S. Okunaka, H. Kameshige, T. Ikeda, H. Tokudome, T. Hisatomi, T. Yamada and K. Domen, Z-Scheme Water Splitting under Near-Ambient Pressure using a Zirconium Oxide Coating on Printable Photocatalyst Sheets, *ChemSusChem*, 2020, **13**, 4906–4910.
- 123 R. Konta, T. Ishii, H. Kato and A. Kudo, Photocatalytic Activities of Noble Metal Ion Doped SrTiO₃ under Visible Light Irradiation, *J. Phys. Chem. B*, 2004, **108**, 8992–8995.
- 124 U. von Luxburg, A tutorial on spectral clustering, *Stat. Comput.*, 2007, **17**, 395–416.
- 125 T. Chugenji, Z. Pan, V. Nandal, K. Seki, K. Domen and K. Katayama, Local charge carrier dynamics of a particulate Ga-doped La₅Ti₂Cu_{0.9}Ag_{0.1}O_{7S5} photocatalyst and the impact of Rh cocatalysts, *Phys. Chem. Chem. Phys.*, 2022, **24**, 17485–17495.
- 126 M. Katayama, D. Yokoyama, Y. Maeda, Y. Ozaki, M. Tabata, Y. Matsumoto, A. Ishikawa, J. Kubota and K. Domen, Fabrication and photoelectrochemical properties of La₅Ti₂MS₅O₇ (M=Ag, Cu) electrodes, *Mater. Sci. Eng. B*, 2010, **173**, 275–278.
- 127 J. Liu, T. Hisatomi, G. Ma, A. Iwanaga, T. Minegishi, Y. Moriya, M. Katayama, J. Kubota and K. Domen, Improving the photoelectrochemical activity of La₅Ti₂Cu₅O₇ for hydrogen evolution by particle transfer and doping, *Energy Environ. Sci.*, 2014, **7**, 2239–2242.
- 128 T. Hisatomi, S. Okamura, J. Liu, Y. Shinohara, K. Ueda, T. Higashi, M. Katayama, T. Minegishi and K. Domen, La₅Ti₂Cu_{1-x}Ag_xS₅O₇ photocathodes operating at positive potentials during photoelectrochemical hydrogen evolution under irradiation of up to 710 nm, *Energy Environ. Sci.*, 2015, **8**, 3354–3362.
- 129 G. Ma, Y. Suzuki, R. Balia Singh, A. Iwanaga, Y. Moriya, T. Minegishi, J. Liu, T. Hisatomi, H. Nishiyama, M. Katayama, K. Seki, A. Furube, T. Yamada and K. Domen, Photoanodic and photocathodic behaviour of La₅Ti₂Cu₅O₇ electrodes in the water splitting reaction, *Chem. Sci.*, 2015, **6**, 4513–4518.
- 130 J. Liu, T. Hisatomi, M. Katayama, T. Minegishi, J. Kubota and K. Domen, Effect of particle size of La₅Ti₂Cu₅O₇ on photoelectrochemical properties in solar hydrogen evolution, *J. Mater. Chem. A*, 2016, **4**, 4848–4854.
- 131 S. Sun, T. Hisatomi, Q. Wang, S. Chen, G. Ma, J. Liu, S. Nandy, T. Minegishi, M. Katayama and K. Domen, Efficient Redox-Mediator-Free Z-Scheme Water Splitting Employing Oxysulfide Photocatalysts under Visible Light, *ACS Catal.*, 2018, **8**, 1690–1696.

- 132 T. Higashi, Y. Shinohara, A. Ohnishi, J. Liu, K. Ueda, S. Okamura, T. Hisatomi, M. Katayama, H. Nishiyama, T. Yamada, T. Minegishi and K. Domen, Sunlight-Driven Overall Water Splitting by the Combination of Surface-Modified La₅Ti₂Cu_{0.9}Ag_{0.1}S₅O₇ and BaTaO₂N Photoelectrodes, *ChemPhotoChem*, 2017, **1**, 167–172.
- 133 J. Yang, D. Wang, H. Han and C. Li, Roles of Cocatalysts in Photocatalysis and Photoelectrocatalysis, *Acc. Chem. Res.*, 2013, **46**, 1900–1909.
- 134 Z. Pan, R. Yanagi, Q. Wang, X. Shen, Q. Zhu, Y. Xue, J. A. Röhr, T. Hisatomi, K. Domen and S. Hu, Mutually-dependent kinetics and energetics of photocatalyst/co-catalyst/two-redox liquid junctions, *Energy Environ. Sci.*, 2020, **13**, 162–173.
- 135 Z. Pan, J. A. Röhr, Z. Ye, Z. S. Fishman, Q. Zhu, X. Shen and S. Hu, Elucidating charge separation in particulate photocatalysts using nearly intrinsic semiconductors with small asymmetric band bending, *Sustain. Energy Fuels*, 2019, **3**, 850–864.
- 136 Q. Xiao, J. Xiao, J. J. M. Vequizo, T. Hisatomi, M. Nakabayashi, S. Chen, Z. Pan, L. Lin, N. Shibata, A. Yamakata, T. Takata and K. Domen, Cocatalyst engineering of a narrow bandgap Ga-La₅Ti₂Cu_{0.9}Ag_{0.1}O₇S₅ photocatalyst towards effectively enhanced water splitting, *J. Mater. Chem. A*, , DOI:10.1039/D1TA08770C.
- 137 T. Chugenji, Z. Pan and K. Katayama, Microscopic Interfacial Charge Transfer at Perovskite/Hole Transport Layer Interfaces Clarified Using Pattern-Illumination Time-Resolved Phase Microscopy, *J. Phys. Chem. C*, 2022, **126**, 7548–7555.
- 138 M. M. Lee, J. Teuscher, T. Miyasaka, T. N. Murakami and H. J. Snaith, Efficient Hybrid Solar Cells Based on Meso-Superstructured Organometal Halide Perovskites, *Science*, 2012, **338**, 643–647.
- 139 J. Y. Kim, J.-W. Lee, H. S. Jung, H. Shin and N.-G. Park, High-Efficiency Perovskite Solar Cells, *Chem. Rev.*, 2020, **120**, 7867–7918.
- 140 X. Hu, X. Zhang, L. Liang, J. Bao, S. Li, W. Yang and Y. Xie, High-Performance Flexible Broadband Photodetector Based on Organolead Halide Perovskite, *Adv. Funct. Mater.*, 2014, **24**, 7373–7380.
- 141 A. Ishii and T. Miyasaka, Direct detection of circular polarized light in helical 1D perovskite-based photodiode, *Sci. Adv.*, 2020, **6**, eabd3274.
- 142 F. Liu, Y. Zhang, C. Ding, S. Kobayashi, T. Izuishi, N. Nakazawa, T. Toyoda, T. Ohta, S. Hayase, T. Minemoto, K. Yoshino, S. Dai and Q. Shen, Highly Luminescent Phase-Stable CsPbI₃ Perovskite Quantum Dots Achieving Near 100% Absolute Photoluminescence Quantum Yield, *ACS Nano*, 2017, **11**, 10373–10383.
- 143 X. Sheng, Y. Liu, Y. Wang, Y. Li, X. Wang, X. Wang, Z. Dai, J. Bao and X. Xu, Cesium Lead Halide Perovskite Quantum Dots as a Photoluminescence Probe for Metal Ions, *Adv. Mater.*, 2017, **29**, 1700150.

- 144 J. Shi, Y. Li, Y. Li, D. Li, Y. Luo, H. Wu and Q. Meng, From Ultrafast to Ultraslow: Charge-Carrier Dynamics of Perovskite Solar Cells, *Joule*, 2018, **2**, 879–901.
- 145 L. M. Herz, Charge-Carrier Dynamics in Organic-Inorganic Metal Halide Perovskites, *Annu. Rev. Phys. Chem.*, 2016, **67**, 65–89.
- 146 Y. Yamada, T. Nakamura, M. Endo, A. Wakamiya and Y. Kanemitsu, Photocarrier Recombination Dynamics in Perovskite CH₃NH₃PbI₃ for Solar Cell Applications, *J. Am. Chem. Soc.*, 2014, **136**, 11610–11613.
- 147 S. D. Stranks, V. M. Burlakov, T. Leijtens, J. M. Ball, A. Goriely and H. J. Snaith, Recombination Kinetics in Organic-Inorganic Perovskites: Excitons, Free Charge, and Subgap States, *Phys. Rev. Appl.*, 2014, **2**, 034007.
- 148 S. D. Stranks, G. E. Eperon, G. Grancini, C. Menelaou, M. J. P. Alcocer, T. Leijtens, L. M. Herz, A. Petrozza and H. J. Snaith, Electron-Hole Diffusion Lengths Exceeding 1 Micrometer in an Organometal Trihalide Perovskite Absorber, *Science*, 2013, **342**, 341–344.
- 149 O. G. Reid, M. Yang, N. Kopidakis, K. Zhu and G. Rumbles, Grain-Size-Limited Mobility in Methylammonium Lead Iodide Perovskite Thin Films, *ACS Energy Lett.*, 2016, **1**, 561–565.
- 150 G. W. P. Adhyaksa, S. Brittman, H. Āboliņš, A. Lof, X. Li, J. D. Keelor, Y. Luo, T. Duevski, R. M. A. Heeren, S. R. Ellis, D. P. Fenning and E. C. Garnett, Understanding Detrimental and Beneficial Grain Boundary Effects in Halide Perovskites, *Adv. Mater.*, 2018, **30**, 1804792.
- 151 J.-W. Lee, S.-H. Bae, N. De Marco, Y.-T. Hsieh, Z. Dai and Y. Yang, The role of grain boundaries in perovskite solar cells, *Mater. Today Energy*, 2018, **7**, 149–160.
- 152 Y. Wang, W.-H. Fang, R. Long and O. V. Prezhdo, Symmetry Breaking at MAPbI₃ Perovskite Grain Boundaries Suppresses Charge Recombination: Time-Domain ab Initio Analysis, *J. Phys. Chem. Lett.*, 2019, **10**, 1617–1623.
- 153 W.-J. Yin, H. Chen, T. Shi, S.-H. Wei and Y. Yan, Origin of High Electronic Quality in Structurally Disordered CH₃NH₃PbI₃ and the Passivation Effect of Cl and O at Grain Boundaries, *Adv. Electron. Mater.*, 2015, **1**, 1500044.
- 154 L. Wang, C. McCleese, A. Kovalsky, Y. Zhao and C. Burda, Femtosecond Time-Resolved Transient Absorption Spectroscopy of CH₃NH₃PbI₃ Perovskite Films: Evidence for Passivation Effect of PbI₂, *J. Am. Chem. Soc.*, 2014, **136**, 12205–12208.
- 155 F. Zheng, X. Wen, T. Bu, S. Chen, J. Yang, W. Chen, F. Huang, Y. Cheng and B. Jia, Slow Response of Carrier Dynamics in Perovskite Interface upon Illumination, *ACS Appl. Mater. Interfaces*, 2018, **10**, 31452–31461.
- 156 E. M. Hutter, J.-J. Hofman, M. L. Petrus, M. Moes, R. D. Abellón, P. Docampo and T. J. Savenije, Charge Transfer from Methylammonium Lead Iodide Perovskite to Organic Transport Materials: Efficiencies, Transfer Rates, and Interfacial Recombination, *Adv. Energy Mater.*, 2017, **7**, 1602349.
- 157 C. S. Ponseca, E. M. Hutter, P. Piatkowski, B. Cohen, T. Pascher, A. Douhal, A. Yartsev, V.

- Sundström and T. J. Savenije, Mechanism of Charge Transfer and Recombination Dynamics in Organo Metal Halide Perovskites and Organic Electrodes, PCBM, and Spiro-OMeTAD: Role of Dark Carriers, *J. Am. Chem. Soc.*, 2015, **137**, 16043–16048.
- 158 Y. Li, J. Shi, B. Yu, B. Duan, J. Wu, H. Li, D. Li, Y. Luo, H. Wu and Q. Meng, Exploiting Electrical Transients to Quantify Charge Loss in Solar Cells, *Joule*, 2020, **4**, 472–489.
- 159 J. Shi, D. Li, Y. Luo, H. Wu and Q. Meng, Opto-electro-modulated transient photovoltage and photocurrent system for investigation of charge transport and recombination in solar cells, *Rev. Sci. Instrum.*, 2016, **87**, 123107.
- 160 G. Xing, N. Mathews, S. Sun, S. S. Lim, Y. M. Lam, M. Grätzel, S. Mhaisalkar and T. C. Sum, Long-Range Balanced Electron- and Hole-Transport Lengths in Organic-Inorganic CH₃NH₃PbI₃, *Science*, 2013, **342**, 344–347.
- 161 N. Droseros, B. Dänekamp, D. Tsokkou, P. P. Boix and N. Banerji, Charge injection and trapping at perovskite interfaces with organic hole transporting materials of different ionization energies, *APL Mater.*, 2019, **7**, 041115.
- 162 K. Pydzińska, J. Karolczak, I. Kosta, R. Tena-Zaera, A. Todinova, J. Idígoras, J. A. Anta and M. Ziólek, Determination of Interfacial Charge-Transfer Rate Constants in Perovskite Solar Cells, *ChemSusChem*, 2016, **9**, 1647–1659.